Xia *et al. Energy Mater* 2022;2:200015
DOI: 10.20517/energymater.2022.13

Energy Materials

Review

Open Access

Carbon-supported single-atom catalysts for advanced rechargeable metal-air batteries

Qing Xia[1,#], Yanjie Zhai[2,#], Lanling Zhao[3], Jun Wang[1,*], Deyuan Li[1], Lili Zhang[4,*], Jintao Zhang[1,*]

[1]Key Laboratory for Colloid and Interface Chemistry, Ministry of Education, School of Chemistry and Chemical Engineering, Shandong University, Jinan 250100, Shandong, China.
[2]Department of Mechanical Engineering, The Hong Kong Polytechnic University, Hung Hom, Kowloon, Hong Kong SAR, China.
[3]School of Physics, Shandong University, Jinan 250100, Shandong, China
[4]Institute of Chemical and Engineering Sciences, A*STAR, 1 Pesek Road, Jurong Island 627833, Singapore.
[#]These authors contributed equally.

***Correspondence to:** Prof./Dr. Jintao Zhang, Key Laboratory for Colloid and Interface Chemistry, Ministry of Education, School of Chemistry and Chemical Engineering, Shandong University, Jinan 250100, No. 27, Shanda South Road, China. E-mail: jtzhang@sdu.edu.cn; Dr. Jun Wang, Key Laboratory for Colloid and Interface Chemistry, Ministry of Education, School of Chemistry and Chemical Engineering, Shandong University, Jinan 250100, No. 27, Shanda South Road, China. E-mail: jw707@sdu.edu.cn; Dr. Lili Zhang, Institute of Chemical and Engineering Sciences, A*STAR, 1 Pesek Road, Jurong Island 627833, Singapore. E-mail: zhang_lili@ices.a-star.edu.sg

How to cite this article: Xia Q, Zhai Y, Zhao L, Wang J, Li D, Zhang L, Zhang J. Carbon-supported single-atom catalysts for advanced rechargeable metal-air batteries. *Energy Mater* 2022;2:200015. https://dx.doi.org/10.20517/energymater.2022.13

Received: 16 Mar 2022 **First Decision:** 11 Apr 2022 **Revised:** 20 Apr 2022 **Accepted:** 26 Apr 2022 **Published:** 12 May 2022

Academic Editors: Yuping Wu, Yuhui Chen **Copy Editor:** Tiantian Shi **Production Editor:** Tiantian Shi

Abstract

To address the fossil energy crisis and environmental problems, the urgent demand for clean energy has promoted the rapid development of advanced rechargeable metal-air batteries based on the redox reaction couples of gases, such as the oxygen reduction, oxygen evolution, carbon dioxide reduction and carbon dioxide evolution reactions. High-efficiency electrocatalysts are highly desirable to enhance the conversion efficiency of these reactions for enhancing battery performance. Significant advances in single-atom catalysts (SACs) on carbon matrices have been witnessed in recent years as attractive and unique systems to improve the electrocatalytic activities for high-performance rechargeable Zn- and Li-air batteries. This review summarizes the latest achievements in the applications of carbon-supported SACs in metal-air batteries, with a particular focus on the rational design of SACs and their fundamental electrocatalytic mechanism at the atomic level. The future development and perspectives of SACs in the field of metal-air batteries are also discussed.

Keywords: Single-atom catalysts, carbon supports, electrodes, electrocatalysis, Zn- and Li-air batteries

INTRODUCTION

The global shift away from fossil- and carbon-based energy has promoted the development of green and renewable energy conversion and storage systems, such as rechargeable batteries based on a metal with oxygen (metal-O_2) or carbon dioxide (metal-CO_2)[1-8]. Among them[9-12], benefiting from the low density of Li metal and the stable chemical properties of Zn, metal-air batteries based on Li or Zn as the anode have a very high energy density and outstanding cycling stability and are therefore considered the most likely next-generation energy storage and conversion devices for electric vehicles[13,14]. In addition, in contrast to the current research on the reduction of CO_2 into CO, formic acid and other products, which requires electrolysis to consume energy, metal-CO_2 batteries, such as aprotic Li-CO_2 and aqueous Zn-CO_2 batteries, use CO_2 as a negative electrode in combination to achieve slow CO_2 fixation/utilization[15-18], while generating electricity instead of consuming electricity. However, these batteries face many challenges in actual applications, such as high overcharge potentials, by-products from decomposition of the electrolyte and poor cycle stability[19-22]. Researchers have found that one of the main reasons for these problems is the slow dynamics of the oxygen reduction reaction (ORR), oxygen evolution reaction (OER), carbon dioxide reduction reaction (CO_2RR) and carbon dioxide evolution reaction (CO_2ER). Thus, research has mainly been focused on catalyst development in order to solve the above-mentioned issue of slow reaction kinetics[23-25].

Precious metals have been found to be the best performing catalysts[26-28]. However, due to their scarcity and high price, there is a constant search for low-cost and sustainable alternatives, such as transition metal oxides[29-32], transition metal chalcogenides[33-35], metal nitrides[36,37] and carbon-based materials[38-40]. In recent years, metal-based nanoparticles (NPs) have received tremendous interest due to their unique mechanical and electrical properties and the synergy of their surface properties, which contribute to their overall behavior. Compared to their bulk counterparts, NPs possess much larger surface areas and quantum size effects. As the size of an NP decreases, the ratio of its exposed surface atoms increases dramatically. The unique surface atomic structure and electronic structure of NPs offer significant potential in catalytic applications[41-43]. More importantly, as the number of atoms of NPs decreases further, nanoclusters are formed, which exhibit enhanced catalytic performance[44-46]. According to the above phenomenon and explanation, the atomic utilization can be maximized with very high catalytic efficiency if the size of the metal is properly controlled down to the atomic level.

Single-atom catalysts (SACs) are commonly composed of a single metal atom and coordinated heteroatoms on the surfaces of carbon materials, metal oxides and others. In addition to carbon materials, the anchoring of metal atoms on non-carbon supports is also efficient in improving the utilization of metal for enhancing electrocatalysis. For example, metal-supported SACs tend to be formed when the radius and bond formation energy of the supported atoms are close to those of the host metal atoms and their electronic structure can be precisely tuned by properly loading single atoms for an efficient HER, OER and ORR. Metal oxides are effective catalysts for the ORR, and it is possible to obtain high-efficiency bifunctional catalysts after loading SACs on them, which can be used as Li-O_2 and Zn-air battery cathodes. In addition, chalcogenides feature higher electrical conductivity and are effective for CO_2 reduction, making them potential matrix materials for loading single atoms in Li- and Zn-CO_2 batteries. Comparatively, carbon materials, such as graphene, carbon nanotubes (CNTs), carbon nanofibers (CNFs), carbon paper and carbon cloth with high surface areas and superior electrical conductivity are normally employed as SAC supports to boost the ORR, OER, CO_2RR and CO_2ER by providing abundant channels for mass transfer and

thus remarkably improving the electrochemical activities. Moreover, the matrix materials also play a critical role in storing discharge products in the batteries, such as Li_2O_2 and Li_2CO_3. For promising practical applications, the energy stored per unit mass or area should be sufficiently high. In this case, carbon matrices exhibit a unique advantage. Compared with metals, oxides, chalcogenides and other compound materials, their mass-specific density is much lower and the preparation processes of porous carbon materials tend to be mature, which can be used to effectively control the pore structures for improving electrocatalytic performance.

In 2011, Qiao *et al.*[47] first deposited a single Pt atom on iron oxide, which was used for CO oxidation. Both experiments and density functional theory (DFT) calculations showed that Pt atoms lowered the CO adsorption energy and activation barrier for CO oxidation. SACs have also been shown to be useful in electrochemical energy conversion and storage[48-50], including the ORR[51-53], OER[54-56], HER[57-59] and CO_2RR[60-62]. For superior catalytic performance, SACs with separated metal atoms dispersed on a conductive carrier represent promising electrode materials and have been increasingly used in Li- and Zn-air batteries in recent years.

In this review, we first give a brief introduction regarding Li- and Zn-air batteries and the geometric and electronic structures of SACs on carbon matrices. We then summarize the recent research progress of the applications of SACs in Li- and Zn-air batteries, with a particular focus on their catalytic mechanism. Finally, the future perspectives for the development of SACs are provided.

COMPARISON OF LI- AND ZN-AIR BATTERIES: ENERGY DENSITY, CELL CONFIGURATIONS AND PRINCIPLES

Energy density

Li-ion batteries are widely used in mobile phones and electric vehicles due to their large capacity and stable cycle performance[63-65]. However, due to their energy density limitations, the working times of mobile phones and the mileages of electric vehicles are reaching a plateau. Therefore, this has stimulated researchers to search for new battery systems with higher energy density, among which metal-air batteries have received widespread attention[66-68]. Since Abraham and Jiang invented rechargeable Li-air batteries in 1996, they have been divided into four types, namely, aprotic, water, hybrid and solid state, which utilize different electrolytes[69,70]. Among them, because of their excellent reversibility, aprotic Li-O_2 batteries have received significant interest. As shown in Figure 1A, Li-air batteries offer the highest theoretical energy density of 11429 Wh kg^{-1}, which is comparable to that of gasoline[71]. In addition, the theoretical energy densities of Al- and Mg-air batteries are also very high, with values of 8076 and 6815 Wh kg^{-1}, respectively, which are five to six times that of Zn-air batteries (1353 Wh kg^{-1}). However, their practical energy density is low due to the large polarization and low voltage. Furthermore, they are difficult to electrochemically charge in alkaline electrolytes, thereby limiting their practical application. In contrast, Zn is more stable and can be charged more successfully in alkaline electrolytes[72-74]. As shown in Figure 1B, the practical energy density of Zn-air batteries has reached 350 Wh kg^{-1}, which is twice that of Li-ion batteries[75]. They also have a very stable working voltage and are the best power sources for advanced hearing aids[76-78], such as BTE, in-ear and ear canal devices. This has resulted in significant industrial interest in the research and development of Zn-air batteries for hearing aids. For example, Revolt recently signed a cooperation agreement with PhonakAG to jointly develop rechargeable Zn-air batteries for hearing aids.

The energy densities of Li- and Zn-CO_2 batteries are also higher than that of Li-ion batteries, with the theoretical energy density of Li-CO_2 batteries reaching 1876 Wh kg^{-1}. Further research into the corresponding carbon dioxide batteries cannot only provide a deeper understanding of the CO_2RR and

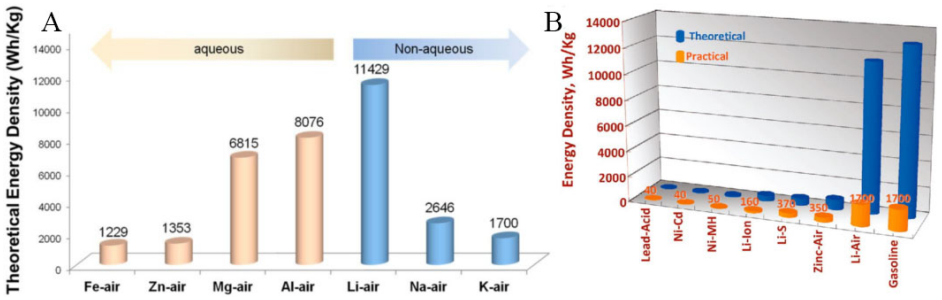

Figure 1. (A) Theoretical energy densities for different types of metal-air batteries. Reproduced with permission: Copyright 2017, American Chemical Society[71]. (B) Gravimetric energy densities (Wh kg^{-1}) for various types of rechargeable batteries compared to that of gasoline. Reproduced with permission: Copyright 2014, American Chemical Society[75].

CO_2ER, but can also promote the study of the corresponding metal-oxygen batteries via an in-depth understanding of the formation and decomposition mechanism of their by-products.

Cell configurations and working principles of Zn- and Li-air batteries

Zn-air batteries

As shown in Figure 2A, the structure of Zn-air batteries is mainly composed of four parts, namely, a metal Zn electrode as the anode, a porous separator, an alkaline electrolyte solution and a cathode porous air electrode[79]. The air cathode is composed of a catalytic layer, a current collecting layer and a gas diffusion layer. A mixture of active material powder and PTFE binder is used to fabricate the catalytic layer. For typical alkaline Zn-air batteries, the electrochemical reactions are shown in Eqs. (1)-(5)[80,81]. During discharge, the oxidation of the Zn anode is combined with hydroxide ions to generate $Zn(OH)_4^{2-}$, which possibly decomposes into ZnO. Simultaneously, oxygen is reduced in the cathode at the catalyst-oxygen-electrolyte 3-phase boundaries. During the charging process of a rechargeable Zn-air battery, the zinc compounds are reduced and deposited as Zn metal with the OER via the desirable four-electron process under external voltages.

$$\text{Anode: } Zn \rightarrow Zn^{2+} + 2e^- \quad (1)$$

$$Zn^{2+} + 4OH^- \rightarrow Zn(OH)_4^{2-} \quad (2)$$

$$Zn(OH)_4^{2-} \rightarrow ZnO + H_2O + 2OH^- \quad (3)$$

$$\text{Cathode: } O_2 + 2H_2O + 4e^- \rightarrow 4OH^- \quad (4)$$

$$\text{Overall: } 2Zn + O_2 \rightarrow 2ZnO \quad (5)$$

Zn-CO_2 batteries

The main components of Zn-CO_2 batteries are a metal Zn anode, a porous air cathode, an electrolyte and bipolar membranes. The bipolar membranes can maintain the stability of the alkaline anolyte and neutral catholyte simultaneously, as well as the dynamic characteristics of ion migration and protons[82]. Compared with inert Li-CO_2 batteries, aqueous Zn-CO_2 batteries provide a proton-coupled electron transfer pathway for CO_2 reduction to value-added carbon-containing products[83-85], including CO, C_2H_4, HCOOH and C_2H_5OH [Figure 2B], as the products of the cathode. For example, Xie *et al.*[86] recently reported a reversible aqueous Zn-CO_2 battery based on CO_2-HCOOH interconversion on a bifunctional Pd cathode. CO_2 was

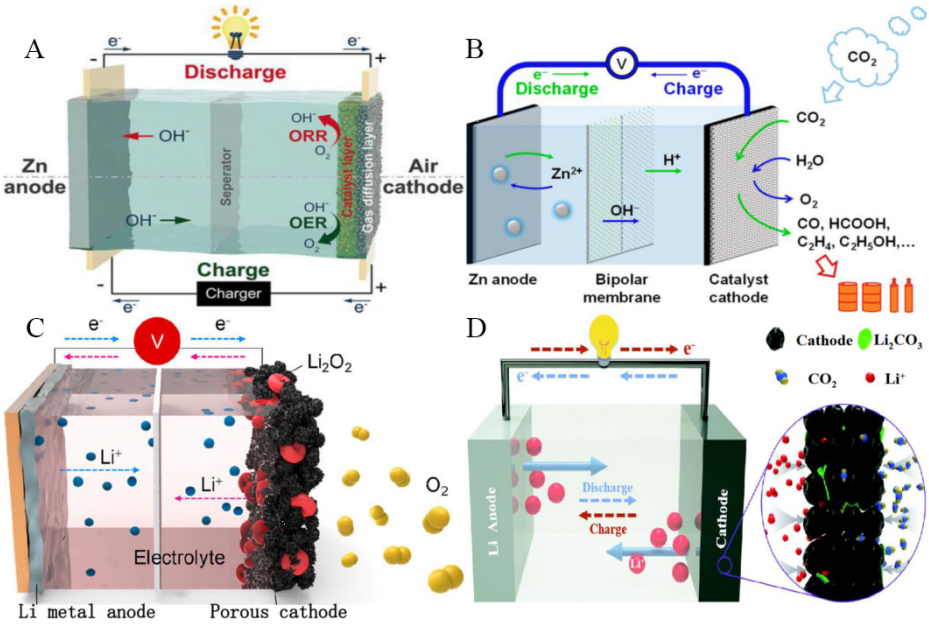

Figure 2. (A) Zn-air battery cell. Reproduced with permission: Copyright 2019, Wiley[79]. (B) Zn-CO_2 battery cell. Reproduced with permission: Copyright 2019, American Chemical Society[82]. (C) Li-O_2 battery cell. Reproduced with permission: Copyright 2020, American Chemical Society[87]. (D) Li-CO_2 battery cell. Reproduced with permission: Copyright 2019, Royal Society of Chemistry[93].

converted to HCOOH on the Pd cathode during the discharge process. During charging, the Pd cathode underwent a reversible HCOOH-to-CO_2 conversion. For Zn-CO_2 batteries, the chemical reactions of different products on the cathode are shown in Eqs. (6)-(10):

$$CO_2 + 2e^- + 2H^+ \rightarrow CO + H_2O \qquad E = -0.11\ V \tag{6}$$

$$CO_2 + 2e^- + 2H^+ \rightarrow HCOOH \qquad E = -0.20\ V \tag{7}$$

$$2CO_2 + 12e^- + 12H^+ \rightarrow C_2H_4 + 4H_2O \qquad E = 0.07\ V \tag{8}$$

$$2CO_2 + 12e^- + 12H^+ \rightarrow C_2H_5OH + 3H_2O \qquad E = 0.08\ V \tag{9}$$

The anode reaction is as follows:

$$Zn + 4OH^- \rightarrow Zn(OH)_4^{2-} + 2e^- \qquad E = 1.20\ V \tag{10}$$

Li-O_2 batteries

A typical non-aqueous Li-O_2 battery consists of three parts, namely, a Li metal anode, an electrolyte solution with a Li salt in an aprotic solution and the cathode consisting of a porous catalyst and a conductive agent [Figure 2C][87]. During the discharge process, the Li in the anode is oxidized to form Li ions, while the oxygen in the cathode is reduced to form superoxide ions at the two-phase interfaces between the electrolyte solution and the cathode. The superoxide ions are then combined with Li ions transported through the electrolyte to form lithium superoxide (LiO_2)[88]. The single-electron transfer electrochemical process or disproportionation reaction leads to the form of lithium peroxide (Li_2O_2)[89]. According to current research on the discharge mechanism of Li-O_2 batteries, the morphology of discharge products is largely controlled

by the solubility of LiO_2 intermediates[70,90]. In strong Li^+ solvated solvents, Li_2O_2 usually forms thin films or small particles through surface mechanisms. In weak Li^+ solvating solvents, large-sized Li_2O_2 particles are formed by solution mechanisms. During the charging process, the products, including LiO_2, are oxidized and decomposed into Li ions, electrons and oxygen. The charge-discharge electrochemical equations are shown below[91]:

$$\text{Li electrode: } Li \rightarrow Li^+ + e^- \quad (11)$$

$$\text{Air electrode: } O_2 + e^- \rightarrow O_2^- \quad (12)$$

$$LiO_2 + Li^+ + e^- \rightarrow Li_2O_2 \quad (13)$$

$$2LiO_2 \rightarrow Li_2O_2 + O_2 \quad (14)$$

$$\text{Overall: } 2Li + O_2 \rightarrow Li_2O_2 \ (E_{OCV} = 2.96\ V) \quad (15)$$

Li-CO_2 batteries

Initial Li-CO_2 battery investigations originated from the effects of CO_2 in Li-air batteries. With O_2/CO_2 combination operating gases, the high discharge capacity is three times that of pure O_2-based batteries[92]. Because of their potential to trap CO_2 and deliver power, further investigations have focused on Li-CO_2 batteries. The configuration of liquid-free Li-CO_2 batteries is shown in Figure 2D. These batteries consist of two electrodes, namely, a Li metal anode and a porous air cathode[93]. During the discharge process, the Li anode loses electrons and releases Li^+ electrolytes, while CO_2 molecules trap electrons and Li ions on the cathode surfaces to form the mixed products of Li_2CO_3 and carbon. During the charging process, Li_2CO_3 and carbon are reversibly decomposed to produce CO_2 and Li ions[94-96]. The electrochemical reaction equations are as follows:

$$\text{Anode: } 4Li \rightarrow 4Li^+ + 4e^- \quad (16)$$

$$\text{Cathode: } 4Li + 3CO_2 + 4e^- \rightarrow 2Li_2CO_3 + C \quad (17)$$

$$\text{Overall: } 3CO_2 + 4Li \rightarrow Li_2CO_3 + C \quad (18)$$

SINGLE-ATOM CATALYSTS

Features

In 2011, Zhang and colleagues[47] first proposed the term "monoatomic catalysis" in their seminal work. In recent years, this has gradually been accepted by the catalytic community and has become a new field in catalysis. SACs, with their catalytic sites dispersed at the atomic level, utilize metal active sites to the greatest extent and usually exhibit ultrahigh activity and selectivity[97,98]. However, as shown in Figure 3, as the particle size of a catalyst is reduced to the atomic scale, the surface free energy increases rapidly and the single atoms tend to aggregate[99,100]. To understand and solve these problems, we need to develop a deeper understanding of the structures of SACs.

Geometric and electronic structures

The strong interaction between a single atom and the surrounding ligands forms a catalytically active site[101]. This structure can be observed by AC-TEM HAADF-STEM AFM[102-104]. As displayed in Figure 4, the factors influencing the geometric structures of SACs on graphene substrates include the number of N

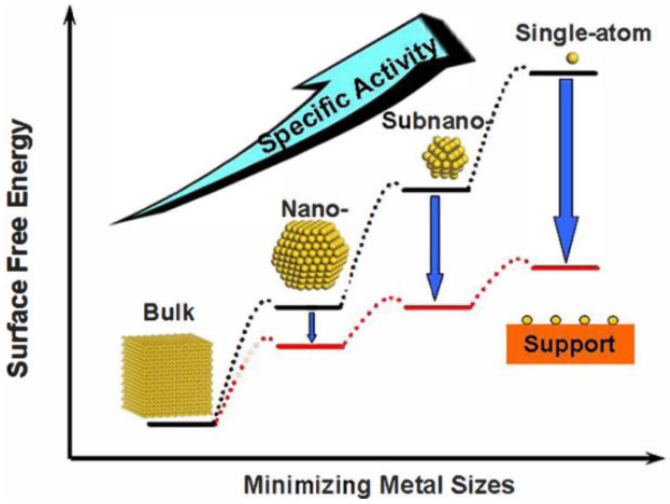

Figure 3. Schematic illustrating the changes in surface free energy and specific activity per metal atom with metal particle size and the support effects on stabilizing single atoms. Reproduced with permission: Copyright 2013, American Chemical Society[100].

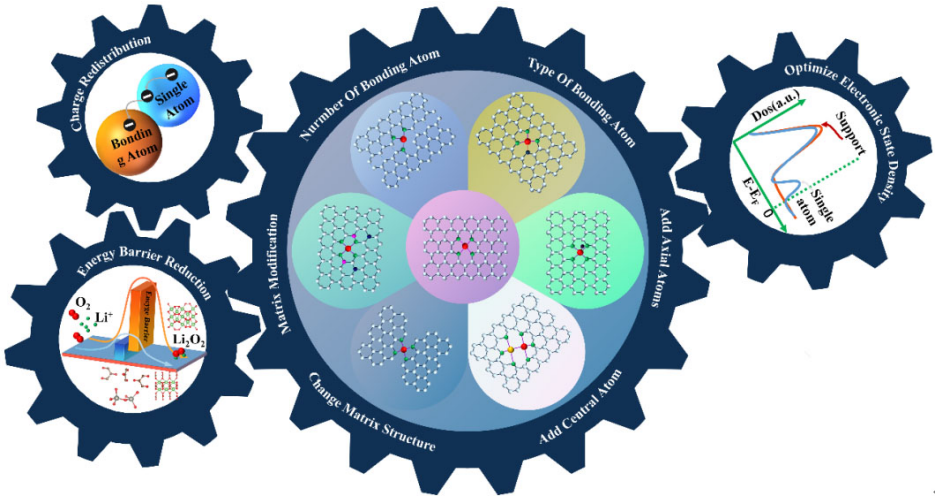

Figure 4. Schematic illustration of different geometric structures of carbon-supported SACs and the function of adjusting the electronic structure.

atoms, the number of metal atoms, the bonding of other atoms (including the axial addition of atoms), the structural change of the matrix and the modification (doping) of the matrix.

When the geometric structure and chemical bond are established, charge transfer between the metal atom and the surrounding atoms occurs due to the difference in chemical potential[105,106]. The adsorption behavior of the catalyst is mainly controlled by the electronic properties of the active sites. Therefore, adjusting the electronic structure of the metal atom by altering the surrounding environment is the most common method to improve the inherent catalytic ability of a SAC[107]. For example, Luo and co-workers[108] conducted a computational search of 17 metal elements based on the model of the coordination of transition metals with four pyridyl nitrogen atoms in a graphene matrix and found that most M-N-Cs showed poor HER catalytic performance because the Gibbs free energy (ΔH) of their hydrogen adsorption is far from 0 eV. Only M-N-Cs with Co, Cr, Fe, Rh and V transition metals were found to be promising

candidates, among which Co-N-C materials show the smallest $|\Delta GGH|$ (0.13 eV) and are therefore predicted to have the best HER activity.

Wang *et al.*[109] demonstrated via a CO_2RR test that a Co-N_2 catalyst with the highest FE_{CO} of 95% at -0.68 V_{RHE} has a much better performance than Co-N_4, which exhibited negligible activity. Furthermore, Pan *et al.*[110] established two FeN_4-type active sites surrounded by different numbers of local carbon atoms, denoted as FeN_4-C_{10} and FeN_4-C_8, respectively. DFT calculations showed that the oxygen adsorption energy increased from -0.95 to -1.67 eV and the OOH dissociation process at the FeO_4-C_8 position only requires an activation energy of 0.2 eV, which is 0.36 eV lower than the activation energy at the FeN_4-C_{10} position. Yuan *et al.*[111] proved that the atomically dispersed Fe-N_x species on B-doped porous carbons have better ORR performance than undoped electrodes through linear sweep voltammetry polarization curves. Ren and co-workers[112] prepared an atom-dispersed Ni-Fe bimetallic center catalyst that showed better CO_2RR performance than the corresponding Ni-Fe single center. These examples undoubtedly illustrate that the electronic structure of SACs is affected by multiple factors, and only when certain conditions are met synergistically can SACs with high catalytic performance be obtained.

APPLICATION OF SINGLE-ATOM CATALYSTS IN METAL-AIR BATTERIES

Application in Zn-air batteries

M-N_x-C structure (M = Fe, Co or Cu)

In recent research reports, it was found that many transition metal center atoms have good ORR/OER properties. In 2017, Specchia *et al.*[113] compared and studied the kinetics of different M-Cs (M = Fe, Co or Cu) in detail and concluded that the oxygen adsorption strength follows the trend of Cu-NC > Fe-NC > Co-NC. Duan *et al.*[114] compared the OER activities of the same active sites (M-N_4C_4) (M = Fe, Co or Ni) and discovered that they follow the order of Ni-N_4C_4 > Fe-N_4C_4 > C_O-N_4C_4. Du and co-workers[115] dispersed Fe atoms on N-doped carbon through a "confined recrystallization" self-template strategy and the mass fraction of Fe reached 1.5%. The high angle annular dark-field STEM image showed a uniform distribution of single atoms [Figure 5A]. The fitting lines of the Fe-NC SACs in R-space confirmed the coordination of Fe-N_4 [Figure 5B]. The authors also studied the reaction path further using DFT calculations. The calculations showed that the ORR follows the association mechanism of O_2 / *OOH / *O / *OH / OH^-, while the OER follows the mechanism of OH- / *OH- / *O / *OOH / O_2 [Figure 5C]. In fact, this is also the reaction pathway of almost all SACs in Zn-air batteries. It is noteworthy that in flexible solid Zn-air batteries, Fe-NC SACs exhibit a high discharge voltage of 1.25 V and excellent cycle performance over 160 cycles at 1 mA cm^{-2}. In addition, Fe-N_4 supported on carbon materials, such as SA-Fe-NHPC[116], Fe/N/C-DT[116] and 3DOM Fe-N-C-900[117], have been synthesized and applied to Zn-air batteries with large peak power density and superior long-term stability.

Ji and co-workers[118] embedded C_O atoms on an N-doped carbon flake array (CoSA@NCF/CNF) using a dipping-carbonation-acidification process. Promising results were obtained when CoSA@NCF/CNF was used in wearable Zn-air batteries. Compared with Co nanoclusters, CoSA@NCF/CNF delivered better ORR and OER performance. The authors established the model [Figure 5D] and the free-energy diagram [Figure 5E] of the CoSA and Co cluster-based ORR through DFT calculations. Under the equilibrium voltage (U = 1.23 V), it was found that the minimized free energy change step was the rate-limiting step (RLS) that defines the limiting potential of the ORR for both catalysts as OH*-OH^- but with a much lower energy required for C_O-N_4/C. At U = 0 V, the RLS was found to be endothermic. These results indicate that monoatomic materials can improve the catalytic performance by reducing the overall oxygen reduction/release reaction barrier. Similarly, Han *et al.*[119] synthesized Co nanoparticles, atomic Co clusters and Co single atoms on N-doped carbon by adjusting the Zn dopant content in a bimetallic ZnCo-ZIF

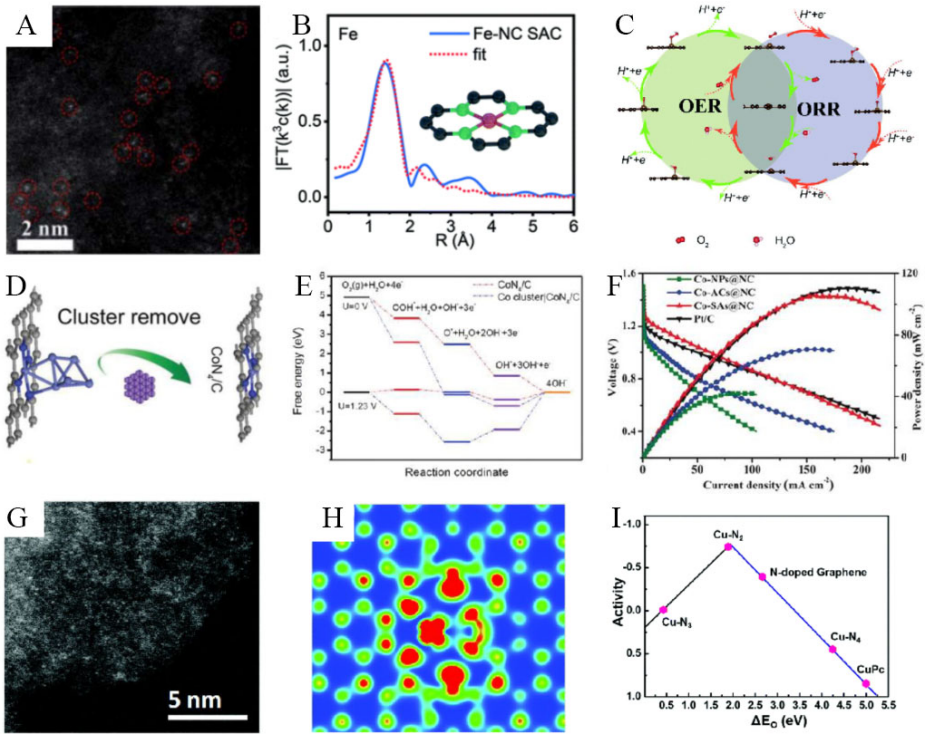

Figure 5. (A) High angle annular dark-field STEM image of Fe-NC SACs. (B) Fitting lines of Fe-NC SACs in R-space with an inset schematic of the Fe-N_4 structure. (C) Schematic of ORR and OER reaction mechanisms on Fe-NC SACs. Reproduced with permission: Copyright 2020, Royal Society of Chemistry[115]. (D) Co-N_4/C and Co cluster|Co-N_4/C models. (E) Free-energy diagram of two models at U = 0 and 1.23 V. Reproduced with permission: Copyright 2019,Wiley[118]. (F) Polarization curves and corresponding power densities of Co-NPs@NC, Co-ACs@NC, Co-SAs@NC and Pt/C-based Zn-air batteries. Reproduced with permission: Copyright 2019, Wiley[119]. (G) HAADF-STEM image of Cu-NrC-60. (H) STM simulation images of Cu-NrC-60. (I) Volcano plot of the relationship between ORR activity and D_{EO} of Cu-N_2, Cu-N_3, Cu-N_4, a CuPc molecule and N-doped graphene. Reproduced with permission: Copyright 2016, Royal Society of Chemistry[120].

precursor. It can be found that the performance of Co SACs is much better than that of the corresponding nanoparticles and nanoclusters [Figure 5F].

As discussed above, modifying the number of surrounding atoms changes the electronic structure of the central atom, thereby affecting the catalytic activity. Wu *et al.*[120] obtained highly doped (8.5 wt.%) and exposed copper(I)-nitrogen [Cu(I)-N] active sites in graphene by paralyzing the coordinated saturated copper phthalocyanine. The HAADF-STEM image is shown in Figure 5G. It can be seen that a large number of Cu atoms are embedded in the graphene matrix. The STM simulation [Figure 5H] shows that the Cu atoms are bonded to two N atoms. The electronic density of states of Cu-N_2, Cu-N_3 and Cu-N_4 were calculated by DFT. The authors found that the Cu-N_2 structure has a moderate binding strength with oxygen species, resulting in good adsorption and desorption capabilities for the ORR. This finding was supported by a volcano plot of the relationship between the ORR activity and Δ_{EO} of different models. We can see that Cu-N_2 has the best activity with moderate Δ_{EO}, which compromises the reaction barriers during the adsorption and desorption steps [Figure 5I]. The authors also calculated the reaction path and energy barrier of Cu-N_2. The removal of *OH needs to overcome an energy barrier of 0.83 eV, which is similar to the theoretical results previously reported on the Pt (111) surface. Yang *et al.*[121] also successfully embedded Cu-N_2 and Cu-N_4 into graphene. Through calculations, they found that Cu-N_2 and Cu-N_4 have potential barriers similar to those of Pt (111) at voltages of 1.23 and 0.4 V, respectively. However, overall, Cu-N_2 exhibits higher activity than Cu-N_4.

Single-atom catalysts on modified carbon matrices

The electronic structure of a SAC can be effectively modified by doping the matrix (heteroatoms or functional groups) to improve the catalytic performance. Sun *et al.*[122] improved the intrinsic activity of the Fe-N_4 active site by introducing a P-O bond, as shown in Figure 6A. The P atom is connected to the N bond on the active site. A water-based Zn-air battery pack equipped with this catalyst showed a significant peak power density of 232 mW cm^{-2} and an excellent cycle performance of 450 stable cycles. The authors also investigated the high catalytic activity through DFT calculations. Figure 6B shows the free-energy diagram of the ORR and OER at 1.23 V on different active sites. Unlike other reports of the limiting step being the first electron transfer ($OO^* + H_2O + e^- = *OOH + OH^-$) step, the limiting step on the P-O/FeN_4-CNS catalyst is the fourth step ($OH^* + 3OH^- + e^- = 4OH^-$). In contrast, in the OER process, the limiting steps are all $O^* + 2OH^- = HOO^* + OH^- + e^-$, with P-O/$FeN_4$-CNS still exhibiting the minimum energy barrier. Figure 6C shows the free energy of the ORR and OER limiting steps of different models. It can be seen that the performance of the OER/ORR increases in the order of FeN_4-CNS < P/FeN_4-CNS < P-OH/FeN_4-CNS < P-O/FeN_4-CNS. These results show that P impurities changed the charge density distribution and electronic structure of Fe active sites, and this demonstrated that the P-O group and FeN_4 displayed a synergistic coupling effect, thereby creating a good surface electronic environment that led to the improved catalytic performance.

Chen and co-workers[123] dispersed a single iron atom on a hollow carbon polyhedron co-doped with phosphorus and sulfur (Fe SAs/NPS-HC) through the Kirkendall effect. A schematic diagram of the structure is shown in Figure 6D. Moreover, Zn-air batteries based on Fe-SAs/NPS-HC showed low overpotentials and stable cycle performance. Figure 6F shows the free-energy diagram of the ORR for Fe-SAs/NPS-C, Fe-SAs/NS-C and Fe-SAs/NC. When U = 0 V, the limiting step on all three active sites is the fourth step. Compared with Fe-SAs/NS-C and Fe-SAs/N-C, the energy barrier on Fe-SAs/NPS-C is the smallest, indicating weaker binding of the OH* intermediate and easier OH^- formation on Fe-SAs/NPS-C. According to the charge density differences [Figure 6E] and the linear relationship between OH* binding energy and Bader charge [Figure 6G], it can be seen that the electron donation of the surrounding sulfur and phosphorus can reduce the positive charge of the metal center Fe (Fe δ+) of Fe-SAs/NPS-C, resulting in the reduced bonding strength of OH*.

Unlike the SACs with a general M-N-C structure in previous reports, Yang *et al.*[124] proved that coordinated oxygen atoms can also play an important role in regulating the inherent catalytic activity of transition metals and the corresponding catalysts are effective in the ORR under alkaline conditions, exhibiting good performance as electrodes in Zn-air batteries. The authors also found through calculations that the Mn-N_3O active center showed the best ORR activity, with its structure shown in Figure 6H. Figure 6I shows the free-energy diagram of the ORR on Mn-N_1O_3, Mn-N_2O_2 and Mn-N_3O_1 surfaces under U = 0.4 V. The rate determination step on the three model surfaces is OH* desorption and the Mn-N_3O_1 model shows the lowest energy barrier (0.73 eV), which is very close to the value of the Pt (111) surface. Figure 6J shows the corresponding density of states (DOS) diagram. The downward shift of the center and the adjacent position of the d-band in the Mn-N_3O_1 model first peak make it an ideal ORR active site. The downshifted position of the d-band center and the adjacent position of the first peak relative to the Fermi level in the Mn-N_3O_1 model showed that the Mn-N_3O_1 surface would have either stronger or weaker adsorption with OH* intermediates, thus endowing itself with a perfect ORR active site.

Bimetallic single-atom catalysts

SACs offer significant potential for many catalytic systems due to their high activity, stability and selectivity regarding the unique electronic structure of their active center with nearly 100% atomic utilization. Recent

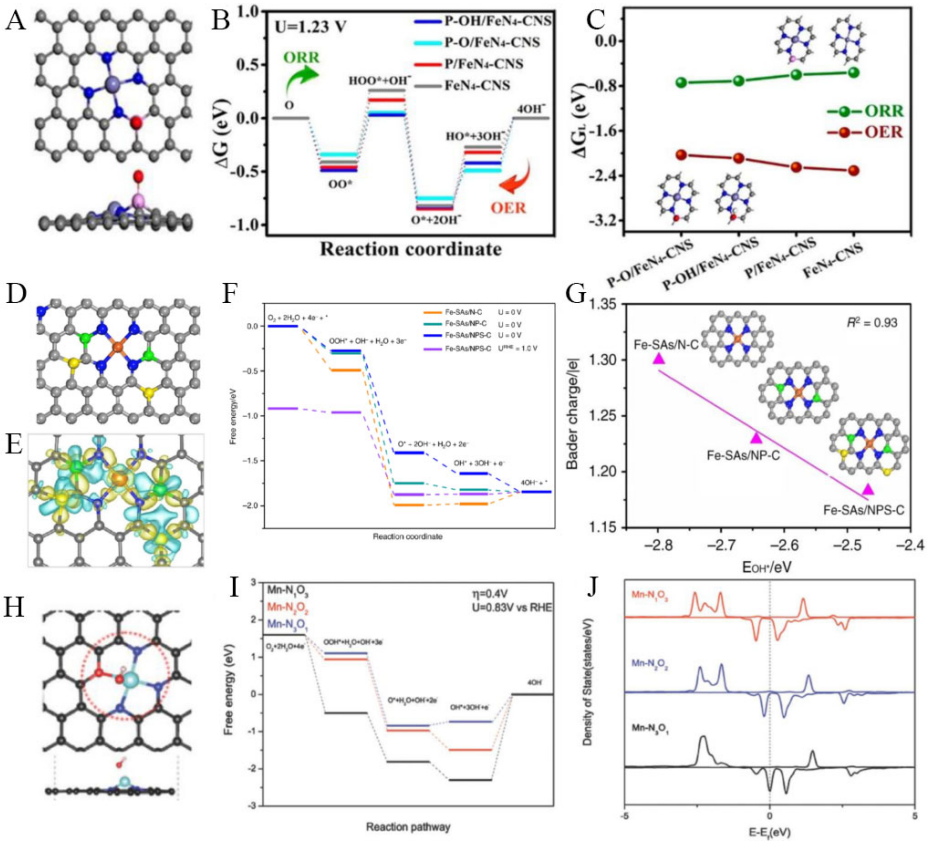

Figure 6. (A) Top and front views of the different models for P-doped FeN_4-CNS. (B) Calculated free-energy diagram of ORR and OER at the equilibrium potential (1.23 V). (C) Free energy of ORR and OER limiting steps for the models. Gray, red, blue, purple, white and pink spheres represent C, O, N, Fe, H and P atoms, respectively. Reproduced with permission: Copyright 2016, American Chemical Society[122]. (D) Schematic model of Fe-SAs/NPS-HC with Fe (orange), N (blue), P (green), S (yellow) and C (gray) atoms. (E) Calculated charge density differences of Fe-SAs/ NPS-C with yellow and blue areas representing charge density increase and reduction, respectively. (F) Free-energy diagram of ORR on different catalysts. (G) The linear relationship between OH* binding energy and Bader charge of different catalysts. Reproduced with permission: Copyright 2018, Springer Nature[123]. (H) Optimized $Mn\text{-}N_3O_1$ structure with ORR intermediate states OH*. The configurations are illustrated both from top and side views. Black, blue, cyan, red and white balls represent C, N, Mn, O and H atoms, respectively. (I) Free-energy diagram of ORR on $Mn\text{-}N_1O_3$, $Mn\text{-}N_2O_2$ and $Mn\text{-}N_3O_1$ surfaces under 0.4 V. (J) Local density of states of Mn d-orbitals in $Mn\text{-}N_1O_3$, $Mn\text{-}N_2O_2$ and $Mn\text{-}N_3O_1$ structures. Reproduced with permission: Copyright 2018,Wiley[124].

studies have shown that the introduction of secondary metal atoms can further enhance the activity of SACs, resulting in enhanced performance.

Han *et al.*[125] embedded binary Co-Ni sites onto N-doped hollow carbon nanocubes (CoNi-SAs/NC) [Figure 7A] through pyrolysis of the primary amine-coated metal-organic framework. Compared with Ni single-atom and N-doped carbon catalysts, the limiting ORR potential of Co-Ni-N is 0.88 eV when U = 0 V [Figure 7B], greater than those of NC (0.14 eV) and Ni-N (0.60 eV). At the equilibrium potential of 1.23 V, the RLS on NC and Ni-N is the hydrogenation of molecular O_2, with energy barriers of 1.09 and 0.63 eV, respectively. While the maximum upslope value of Co-Ni-N is further reduced to 0.35 eV, the RDS becomes the protonation of OH*, which shows that Co-Ni-N has the best ORR capability. During the OER process with a potential of 1.57 V [Figure 7C], OH* adsorption is the RDS on NC and Ni-N with potential barriers of 1.43 and 0.97 eV, respectively, while co-Ni-N can effectively promote the reaction by reducing the energy barrier to 0.69 eV, indicating that Co-Ni-N has the best OER capability. When Co-Ni-N was used as an electrode material in rechargeable Zn-air batteries, it showed lower overpotentials (1.16 and 2.05 V at 10 mA cm^{-2}) than those of Pt/C-IrO_2 (1.17 and 2.12 V at 10 mA cm^{-2}).

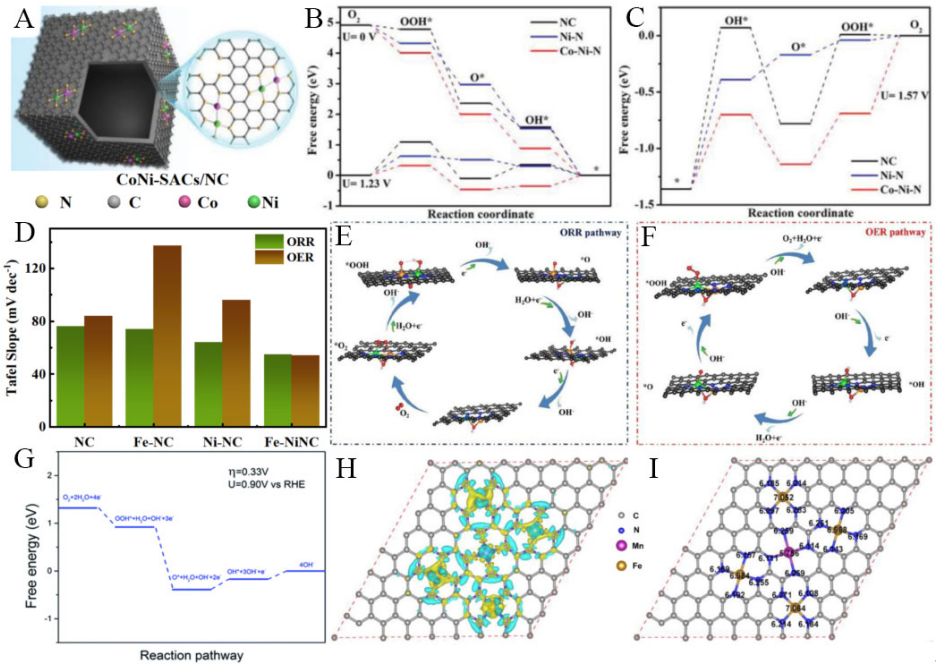

Figure 7. (A) Structure of CoNi-SAs/NC. Free-energy diagrams of (B) two models at 0 and 1.23 V and (C) OER processes on NC, Ni-N and Co-Ni-N at 1.57 V. Reproduced with permission: Copyright 2019, Wiley[125]. (D) Overall bifunctional performance for different catalysts based on Tafel slope in 1 M KOH/0.1 M O_2-saturated KOH. Proposed mechanisms for (E) ORR and (F) OER. Black, blue, green, golden, red and pink balls represent C, N, Ni, Fe, O and H atoms, respectively. Reproduced with permission: Copyright 2020, Elsevier[126]. (G) Free-energy diagram of ORR on Fe, Mn-N/C under an 0.33 V overpotential. (H) Differential charge density illustrating the increase (olive color) and decrease (cyan color) in electron distributions. (I) Bader charge analysis. Reproduced with permission: Copyright 2018, Royal Society of Chemistry[127]. ORR: oxygen reduction reaction; OER: oxygen evolution reaction.

In addition, Zhu *et al.*[126] explained the superior performance of SACs with bimetallic atoms from the perspective of atomic bonds. They used a simple one-step two-solvent impregnation route to embed Fe-Ni bimetallic pairs into nitrogen-doped carbon hollow spheres (Fe-NiNC). The Fe-NiNC catalyst showed better overall bifunctional performance than NC, Fe-NC and Ni-NC [Figure 7D]. The authors compared the ORR and OER activities of Fe-NiNC and Fe-NC through DFT calculations and found an interesting phenomenon. The ORR activity of Fe-NC is similar to that of Fe-NiNC, but the OER activity is much lower. The reason for this is shown in Figures 7E and F. For Fe-NiNC, in the first electron transfer in the ORR process, the O-O bond is disconnected from the OH adsorbed on the Ni atom and O is chemically adsorbed on the Fe atom. The latter process is the same as in the single-atom Fe-NC. While in the OER process, in the presence of the OH ligand bridging Fe-Ni atoms, all intermediates are preferentially adsorbed on Ni. In addition, the physically mixed FeNC+NiNC samples were used for ORR and OER performance testing and showed similar performance to Fe-NC. This indicates that Fe and Ni act as the active centers for the ORR and OER, respectively. Therefore, the catalyst containing bimetallic metal atoms exhibited better bifunctional performance (ORR and OER).

Gong and co-workers[127] dispersed Fe and Mn atoms on porous carbon through the one-step pyrolysis of a metal-organic framework (ZIF-8) and delivered excellent ORR performance when used as an electrode. The discharge curve shows that the change in output voltage is negligible at 20 mA cm^{-2} for 23000 s (6.4 h). As shown in the free-energy diagram of Figure 7G, the RLS of Fe, Mn-N/C is the protonation of O* and lower

energy (0.22 eV) is required than that of Fe -N/C (0.36 eV). According to Bader charge analysis [Figures 7H and I], the Fe and Mn atoms act as electron donors, while N atoms act as electron acceptors. This unique electron donor-acceptor characteristic can alter the electronic structure of Fe, Mn-N/C, thereby reducing the ORR overpotentials.

Application in Zn-CO_2 batteries

As shown in Figure 8A, Wang *et al.*[17] used a gas diffusion strategy and one-step thermal activation method to insert Fe atoms into N-doped porous carbon polyhedra and adjust the pyrolysis temperature to control the number of nitrogen atoms bonded to Fe atoms to obtain optimized Fe_1NC/S_1-1000 (with 3 N atom bonds) samples. A maximal power density of 0.6 mW cm^{-2} was obtained when used in a Zn-CO_2 battery. The authors found that Fe_1NC/S_1-1000 has better CO_2ER catalytic activity than Fe_1NC/S_1-800 (the coordination number of N atoms is 3.8) and Fe_1NC/S_1-900 (the coordination number of N atoms is 3.3). By constructing a model [Figure 8B], the authors calculated the Fe-N_4, Fe-N_3 and Fe-N_3V CO_2ER reaction path energies [Figure 8C]. It was found that the Fe-N_3 active center can significantly reduce the energy barrier of intermediate *COOH and CO generation, thereby improving its CO_2ER performance.

Zheng and co-workers[128] obtained a high-efficiency Zn-CO_2 battery catalyst with Cu-N_2 active sites dispersed on graphene by pyrolyzing the graphene-supported precursor in a high-temperature N_2 atmosphere. FT-EXAFS fitting results confirmed the existence of Cu-N_2 [Figure 8D] and the electrode with Cu-N_2 as the active site has better CO_2ER performance than the electrode with Cu-N_4 as the active site. Zn-CO_2 with Cu-N_2/GN as the catalyst can provide a peak power density of 0.6 mW cm^{-2}. According to DFT calculations, Cu-N_2 requires less energy to capture CO_2 than Cu-N_4. In addition, smaller energy is needed for the intermediate step from *CO_2 to *COOH [Figure 8E] on Cu-N_2 center, explaining the superior CO_2ER activity of Cu-N_2/GN. A series of single metal atoms on N-doped carbon (SAs-MC-N, M = Fe, Co, Ni or Cu) was screened through a one-step in-situ pyrolysis method with the active center structure of M-N_4. The CO_2ER activity follows the order of Ni > Fe > Cu > Co [Figure 8F]. An integrated Zn-CO_2 battery assembled with SAs-Ni-N-C as the cathode delivered a maximum CO_{FE}. of 93.3% with a peak power density of 1.4 mW cm^{-2}. In addition, Yang *et al.*[129] designed and synthesized Ni-N and P-O co-doped graphene (NiPG) as a multifunctional catalyst. A dual-mode Zn-CO_2/Zn-O_2 battery was made with NiPG as the electrode, which can function by supplying either CO_2 or O_2. This advanced the Zn-air battery through the novel design of a multifunctional electrocatalyst and dual-mode batteries.

Applications in Li-O_2 batteries

Wang *et al.*[130] successfully embedded cobalt atoms in ultrathin nitrogen-rich carbon (Co-SAs/NC) through a green gas migration-capture strategy, and it showed an ultralow overpotential (0.4 V) in Li-O_2 batteries [Figure 9B]. As shown in Figure 9A, the Co-SAs/NC electrode exhibits a very low overpotential because the Co atom bonded to the nitrogen atom has a stronger adsorption capacity for LiO_2. Thus, in the ORR process, it will generate uniform nanoscale Li_2O_2, which is easily decomposed in the OER process. In contrast, Co nanoparticles are prone to form agglomerated large-scale Li_2O_2, which not only increases the overpotential during decomposition, but also contains residual Li_2O_2, leading to a decreased electrochemical performance.

In a report by Shui *et al.*[131], Fe atoms were evenly distributed on the carbon support and were bound by nitrogen and oxygen [Figure 9C], with low overpotentials obtained because of the higher boundary between the SAC and the reduced electron and mass barrier by lithium oxide precipitation. There is no doubt that single atoms play a strong role in regulating the formation and decomposition of Li_2O_2. Song and co-workers[132] synthesized a cobalt atom electrocatalyst (N-HP-Co SACs) for Li-O_2 batteries through a polymer encapsulation strategy and showed good cycle stability (218 d). The authors found that its discharge product

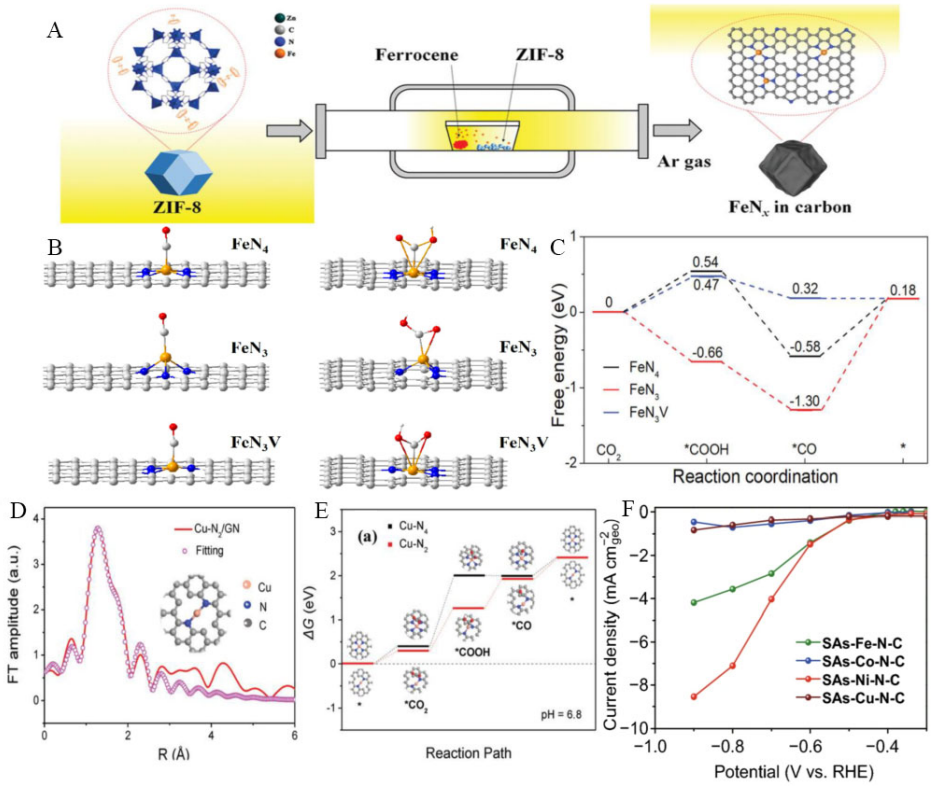

Figure 8. (A) Schematic illustration of synthetic procedure for gas diffusion strategy. (B) Optimized atomic structures for *CO and *COOH intermediates absorbed on FeN_4, FeN_3 and FeN_3V models. Yellow, blue, grey and red balls represent Fe, N, C and O atoms, respectively. (C) Calculated free-energy diagrams for CO_2ER pathway of FeN_4, FeN_3 and FeN_3V moieties. Reproduced with permission: Copyright 2020, Wiley[17]. (D) FT-EXAFS fitting results of Cu-N_2/GN. (E) DFT-based free-energy profile for the optimized Cu-N_2 and Cu-N_4 models during the CO_2ER. (F) Geometric surface area-normalized partial current density for CO production of different catalysts. Reproduced with permission: Copyright 2019, Wiley[128].

is micron-sized and the growth mechanism of the flower-like Li_2O_2 is shown in Figure 9D. The Co atom bonded to the nitrogen atom provides more active sites for Li_2O_2. Under the enhanced solvation-mediated mechanism (E_{ads} = -1.03 eV, the adsorption energy of Li_2O_2 on Co-N_4), the N-HP-Co SACs could provide more nucleation sites, which are conducive to the formation of small nanosheets and further self-assembled to form large sheets. This kind of Li_2O_2 can be completely decomposed at a lower charge voltage, which is an important reason for the good cycle performance of the electrode.

Furthermore, Hu *et al.*[133] used a MOF-assisted space confinement and ion substitution strategy to successfully embed Ru atoms on N-doped porous carbon and optimized the content of Ru atoms ($Ru_{0.3}$ SAs-NC). The electrode showed good ORR and OER catalytic performance. The TEM and HAADF-STEM images are shown in Figure 9E. The isolated Ru atoms are highly dispersed on the porous carbon. The charge density difference [Figure 9F] of $Ru_{0.3}$ SAs-NC was found by DFT calculations, indicating that the Ru-N_4 showed rich charge transfer. Its DOS diagram [Figure 9G] also shows that Ru significantly contributed to the valence band and conductance of the $Ru_{0.3}$ SAs-NC system. Therefore, the surface of $Ru_{0.3}$ SAs-NC is more active/stable than that of the pyrolytic ZIF-8 surface. A similar study involved the loading of single-atom Pt onto porous ultrathin g-C_3N_4 nanosheets (Pt-CNHS)[134]. Figure 9H shows the DOS spectrum of Pt-CNHS. Compared with CNHS, Pt-CNHS shows a narrower band gap, which is attributed to the existence of Pt 5d electrons. The charge distributions of a single Pt atom and CNHS are both abundant and uniform. However, the charge distribution of a single Pt atom on CNHS changed significantly. The

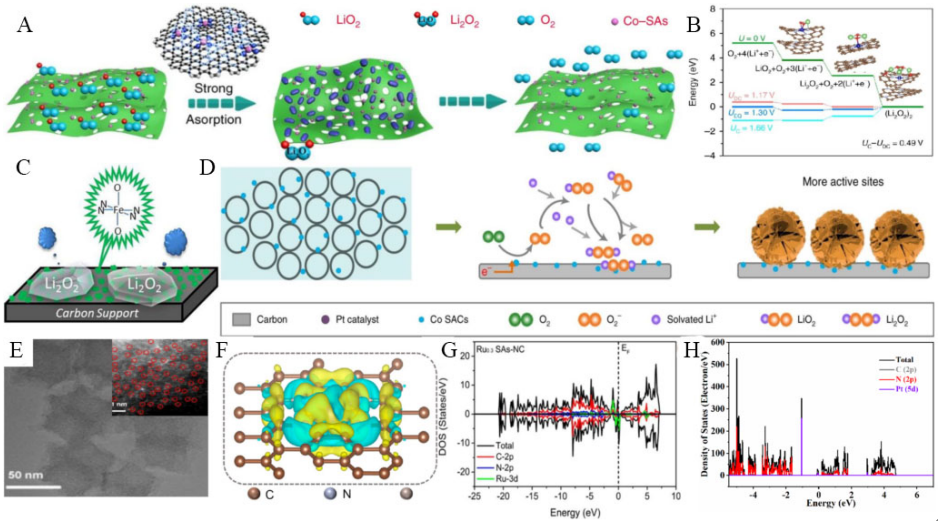

Figure 9. (A) Schematic of working mechanism for Co-SAs/N-C electrodes. (B) Calculated free-energy diagrams for discharge-charge reactions on the active surface of Co-SAs/N-C. Reproduced with permission: Copyright 2020, Springer Nature[130]. (C) Structure of Fe/N/C Composite. Reproduced with permission: Copyright 2012, American Chemical Society[131]. (D) Discharge mechanism of N-HP Co SACs in Li-O_2 batteries. Reproduced with permission: Copyright 2020, Springer Nature[132]. (E) TEM and HAADF-STEM images of $Ru_{0.3}$ SAs-NC with (F) its charge density distribution and (G) total and partial DOS. Reproduced with permission: Copyright 2020, American Chemical Society[133]. (H) DOS of Pt-CNHS. Reproduced with permission: Copyright 2020, Elsevier[134].

charge distribution of the adjacent CNHS also altered slightly, indicating that a single Pt atom strongly interacted with CNHS to form a stable and highly active structure. Simultaneously, it can be seen that the Pt atom has an unbalanced charge distribution to generate local electric fields, which could cause a local built-in driving force that strongly promotes effective electron and ion transmission in the electrode.

Applications in Li-CO_2 batteries

In recent years, SACs have also shown promising performance for the conversion of CO_2 to CO and thus attracted widespread attention. However, there is only a few relevant reports on the practical application of SACs as cathode catalysts for Li-CO_2 batteries. Hu *et al.*[135] successfully implanted single iron atoms into N- and S-doped porous graphene [Figure 10A], which showed high Li-CO_2 battery efficiencies with a low potential gap (1.17 V) and excellent cycle performance (200 cycles). The porous hierarchical architecture features a large surface area and exhibits abundant free space throughout the interconnected framework, in which the pyridine divalent nitrogen atoms at the edge of the graphene anchor the single iron atoms to form many "Fe-N_x" moieties. As shown in Figure 10C, it was calculated and experimentally verified that this composite catalyst delivered the highest catalytic activity compared with those of its counterparts. It is demonstrated that the co-doping of N and S and the presence of the "Fe-N_4" moieties in the carbon skeleton [Figure 10B] would lead to the charge and spin redistribution. This could result in the fast charge transfer between the carbon atoms and the heteroatoms, thereby enabling excellent catalytic performance towards CO_2 reduction and evolution for Li-CO_2 batteries.

Zhang *et al.*[136] anchored 5.3% Co atoms on graphene oxide (adjacent Co/GO), in which adjacent atomic dispersion was maintained, as clearly depicted in its HAADF-STEM image of Figure 10F. The positive shift of absorption edge peaks in Figure 10D and the Co-Co bond centered at 1.90 Å in Figure 10E of the catalysts also indicates that Co particles appear in the form of distributed atoms. DFT calculations were applied to study the stability of Li_2CO_3 intermediates on the surface of GO, SA Co/GO and dimer Co/GO. Interestingly, among the three catalysts, dimer Co/GO shows the lowest adsorption energy of -3.79 V

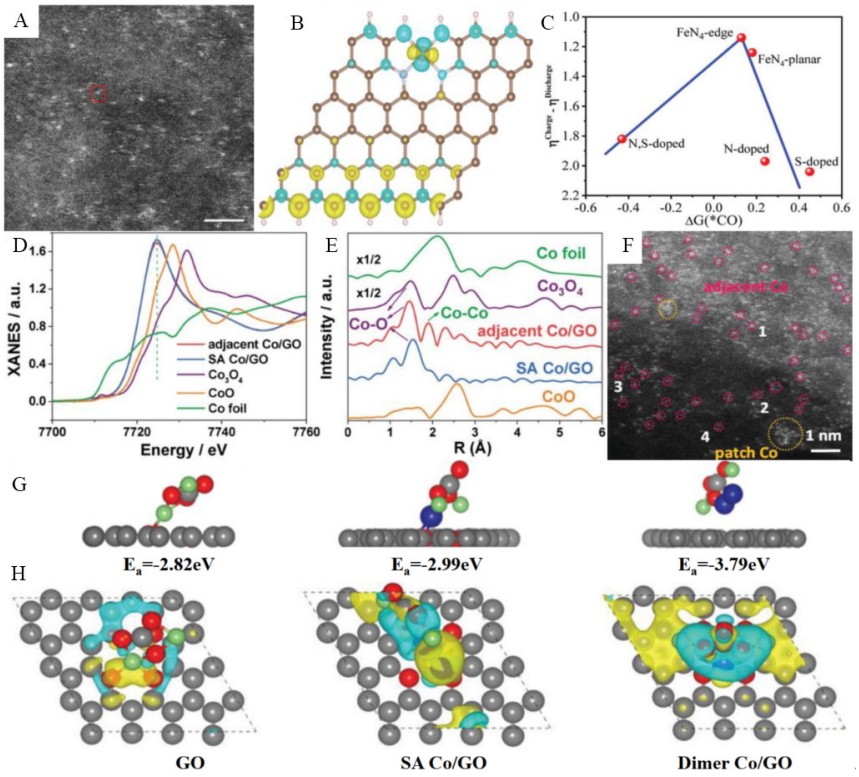

Figure 10. (A) Atomic-resolution STEM images of Fe-ISA/N, S-HG. (B) Spin density distribution of edged "FeN_4" moiety in the carbon skeleton. (C) Adsorption energy of *CO (G*CO) as a function of the overpotential (η_{Charge}-$\eta_{Disharge}$) on the above catalysts. Reproduced with permission: Copyright 2020, Wiley[135]. (D) XANES spectra at the Co K-edge of SA Co/GO, adjacent Co/GO, Co_3O_4, CoO and Co foil. (E) Fourier transforms of Co K-edge of SA Co/GO, adjacent Co/GO, Co_3O_4, CoO and Co foil. (F) HAADF-STEM image of adjacent Co from adjacent Co/GO. (g) Side views and (h) charge density differences of Li_2CO_3 adsorbed on graphene oxide, single cobalt atom and dimer cobalt, respectively. Purple, green, gray and red balls represent Co, Li, C and O, respectively. Reproduced with permission: Copyright 2019, Wiley[136].

[Figure 10G] and the largest equivalent surface in Figure 10H. These findings indicate that the dimer Co could effectively capture Li_2CO_3 and promote the electrocatalytic reactions during cycling, which result in superior Li-CO_2 battery performance of the adjacent Co/GO catalyst.

Tables 1[17,115-128,137-152] and Tables 2[130,132-136] list the recent research progress of the applications of SACs in Li- and Zn-air batteries.

SUMMARY AND PERSPECTIVES

Compared with nanoparticles and nanoclusters, SACs undoubtedly exhibit superior catalytic performance. In this review, we briefly introduce the structural characteristics of Li- and Zn-air batteries and SACs, focusing on the applications of SACs in Li- and Zn-air batteries and the catalytic mechanism of SACs in Li- and Zn-air batteries. The limitations of current research are also discussed. Finally, a perspective is included highlighting the potential and challenges for the future development of SACs in Li- and Zn-air batteries.

Most of the recent reports on SACs as cathode catalysts are based on doping single atoms into N-doped carbon-based materials. Among them, in the category of single-metal SACs, most of the research reports employed M-N_x as the active sites with Fe and Co as the central atoms. On the basis of these reports, some reports provide new ideas, such as doping other atoms, such as S, P and O on the N-doped carbon matrix,

Table 1. Comparison of electrocatalytic performance based on carbon-supported SACs for Zn-air/CO_2 batteries reported in this review

Materials	Peak power density	Open-circuit voltage	Cycles or hours/current density	Ref.
Zn-air batteries				
P-O/FeN_4-CNS	232 mW cm^{-2}	1.50 V	450 cycles/25 mA cm^{-2}	[122]
NC-Co SA	20.9 mW cm^{-2}	1.411 V	125/-	[137]
Fe SAs/ MC(950)	-	1.52 V	-	[138]
SA-Fe-NHPC	266.4 mW cm^{-2}	1.52 V	240 h/20 mA cm^{-2}	[116]
Co SA@NCF/CNF	-	1.41 V	90 cycles/6.25 mA cm^{-3}	[118]
Co-POC	78.0 mW cm^{-2}	-	200 cycles/2.0 mA cm^{-2}	[139]
Ni single atoms/ cluster-C	83.8 mW cm^{-2}	1.35V	258 cycles/2.0 mA cm^{-2}	[140]
Co/N/O tri-doped graphene	152 mW cm^{-2}	1.44 V	18 cycles/1.0 mA cm^{-2}	[141]
Mn/C-NO	120 mW cm^{-2}	-	-	[124]
SCoNC	194 mW cm^{-2}	1.49 V	20 h/5.0 mA cm^{-2}	[142]
Co-SAs@NC	105.3 mW cm^{-2}	1.46 V	50 cycles/1.0 mA cm^{-2}	[119]
Fe-N_4 SAs/NPC	232 mW cm^{-2}	-	108 cycles/2.0 mA cm^{-2}	[143]
CuSA@HNCNx	212 mW cm^{-2}	1.51 V	1800 cycles/10.0 mA cm^{-2}	[144]
EA-Co-900	73 mW cm^{-2}	1.37 V	100 h/20.0 mA cm^{-2}	[145]
Cu-NrC-60	210 mW cm^{-2}	-	100 h/20.0 mA cm^{-2}	[120]
Fe-NC SA	180 mW cm^{-2}	1.424 V	160 cycles/20.0 mA cm^{-2}	[115]
Fe/N/C-DT	220 mW cm^{-2}	1.451 V	-	[117]
Fe-NCF	145 mW cm^{-2}	1.48 V	100 cycles/2.0 mA cm^{-2}	[146]
CoN_4/NG	28 mW cm^{-2}	1.51 V	100 h/10.0 mA cm^{-2}	[147]
3DOM Fe-N-C-900	235 mW cm^{-2}	1.45 V	100 h/5.0 mA cm^{-2}	[148]
Cu-N_x-C	160 mW cm^{-2}	-	-	[121]
Fe-N/C-700	73 mW cm^{-2}	1.53 V	-	[149]
Fe-SAs/NPS-HC	195.0 mW cm^{-2}	1.45 V	500 cycles/5.0 mA cm^{-2}	[123]
A-Co@CMK-3-D-	162 mW cm^{-2}	-	45 h/10.0 mA cm^{-2}	[150]
CoNi-SAs/NC	101.4 mW cm^{-2}	1.45 V	95 cycles/5.0 mA cm^{-2}	[125]
(Fe,Co)/CNT	260 mW cm^{-2}	1.63 V	-	[151]
Mn-N/C-900	140 mW cm^{-2}	1.45 V	6.4 h/20.0 mA cm^{-2}	[127]
Fe-NiNC-50	220 mW cm^{-2}	1.41 V	100 h/2.0 mA cm^{-2}	[126]
	105.3 mW cm^{-2}			
Zn-CO_2 batteries				
Cu-N_2/GN	0.62 mW cm^{-2}	-	120 cycles/1.0 mA cm^{-2}	[128]
Fe_1NC/S1-1000	0.6 mW cm^{-2}	0.727 V	72 cycles/0.5 mA cm^{-2}	[17]
SAs-Ni-N-C	1.4 mW cm^{-2}	-	32 h/1.0 mA cm^{-2}	[152]

or obtaining new active sites, or using bimetal doping to better improve ORR, OER and CO_2RR performance. Although researchers are trying to alter the electronic structure in these ways to obtain catalysts that facilitate catalytic reactions, it is more likely that success will be achieved in permutations. The construction of a large database of SACs, classified by matrix and single-atom types, and the consolidation of a large amount of electronic structure information would be highly convenient for future SACs applications.

For SACs, DFT calculations have shown that the ORR follows the association mechanism of O_2 - *OOH - *O - *OH - OH, while the OER goes on through the mechanism of OH - *OH - *O - * OOH - O_2. SACs can change the ORR, OER and CO_2RR RLSs, mostly to reduce the energy barriers of O_2, CO_2 adsorption and the

Table 2. Comparison of electrocatalytic performance based on carbon-supported SACs for Li-O_2/CO_2 batteries reported in this review

Materials	Overall potential gap/current density	1st discharge capacity/current density	Cycles or hours/current density-fixed capacity	Ref.
Li-O_2 batteries				
$Ru_{0.3}$ SAs-NC	0.55 V/0.02 mA cm^{-2}	13424 mA h g^{-1}/0.02 mA cm^{-2}	60/0.02 mA cm^{-2}-1000 mAh g^{-1}	[133]
Pt-CNHS	-	13843 mA h g^{-1}/200 mA g^{-1}	100/100 mA g^{-1}-600 mAh g^{-1}	[134]
N-HP-Co SACs	-	14777 mA h g^{-1}/100 mA g^{-1}	261/100 mA g^{-1}-1000 mAh g^{-1}	[132]
Co-SAs/N-C	0.40 V/200 mA g^{-1}	17160 mA h g^{-1}/200 mA g^{-1}	260/400 mA g^{-1}-1000 mAh g^{-1}	[130]
Li-CO_2 batteries				
Adjacent Co/GO	-	17358 mA h g^{-1}/100 mA g^{-1}	100/100 mA g^{-1}-1000 mAh g^{-1}	[136]
Fe-ISA/N,S-G	1.17 V/100 mA g^{-1}	23174 mA h g^{-1}/100 mA g^{-1}	200/1000 mA g^{-1} -1000 mAh g^{-1}	[135]

removal of *OH. In Li-O_2 batteries, SACs can effectively tune the structure and morphology of Li_2O_2 to reduce overpotentials. There is no doubt that SACs in Li- and Zn-air batteries deliver very good performance and researchers have made good progress in the catalytic mechanism of SACs, but there are also some problems due to the lack of effective *in situ* characterization techniques and the unclear electrochemical conversion mechanism of SAC materials in advanced batteries systems. Most studies on mechanism analysis use calculation methods, including DFT, to obtain the reaction energy barrier and simulate the transformation kinetics of the corresponding device. The parameter setting difference in the calculation process determines the accuracy of the calculation results. If incorrect modeling is encountered, it is difficult to achieve convergence.

Our vision seems to be limited to carbon-based materials. In fact, single-atom metals can also be doped on different substrates, such as oxides and selenides. The electrical conductivity of the substrate would be sufficiently high for electrocatalytic applications. In fact, some substrates show special functions in battery reactions. For example, when CeO_2 is used as the substrate, the oxygen in its lattice can be involved in the ORR and OER, as an oxygen pump to reduce the reaction overpotentials. For example, the layered materials, MoS_2 and $MoSe_2$, are considered as excellent carriers and their (002) crystal face edges would contribute to extremely superior electrocatalytic performance. Moreover, the electrical conductivity of such a matrix can be improved by a series of methods, such as phase transformation and the construction of heterostructures. It is proposed that single-atom metals may be developed to form tri-metal doping or even four-atom clusters in the future, and they would eventually be expected to be deposited onto other substrates.

The lack of mass production technology for SACs has been a major impediment to their industrial applications. Currently, one-step annealing, co-precipitation and impregnation methods are widely used due to their ease of operation and potential for mass production, but the aggregation commonly leads to the formation of nanoparticles and metal clusters during operation. Therefore, it is necessary to explore facile synthesis processes for high-density, high-purity and large-scale SACs. Recently, the large-scale preparation of ultrahigh-density SACs (kilogram scale) for a variety of metals was developed by a combination of impregnation and two-step annealing process and other methods[153]. In particular, the single atoms with high mass loading were also directly anchored onto different carriers, such as carbon skeletons, oxides and nitrides. These advanced synthesis techniques demonstrate that SACs are expected to be used in industrial applications and would also contribute significantly to the development of Zn- and Li-air batteries.

DECLARATIONS

Authors' contributions

Conception of the study: Zhang J, Wang J, Zhang L
Analysis and manuscript preparation: Xia Q, Zhai Y
Performed the analysis with discussions: Li D, Zhao L

Availability of data and materials

Not applicable.

Financial support and sponsorship

This work was supported for collection, analysis and interpretation of data, and writing of the manuscript by the National Natural Science Foundation of China (22175108), the Natural Scientific Foundation of Shandong Province (ZR2020JQ09), the China Postdoctoral Science Foundation (No.2020M672054), the Guangdong Basic and Applied Basic Research Foundation (No. 2021A1515111124), the Natural Science Foundation of Shandong Province (No. ZR2020QB122), and the Young Scholars Program of Shandong University (No. 2019WLJH21).

Conflicts of interest

All authors declared that there are no conflicts of interest.

Ethical approval and consent to participate

Not applicable.

Consent for publication

Not applicable.

REFERENCES

1. Asadi M, Sayahpour B, Abbasi P, et al. A lithium-oxygen battery with a long cycle life in an air-like atmosphere. *Nature* 2018;555:502-6. DOI PubMed
2. Gourdin G, Xiao N, McCulloch W, Wu Y. Use of polarization curves and impedance analyses to optimize the "triple-phase boundary" in K-O_2 batteries. *ACS Appl Mater Interfaces* 2019;11:2925-34. DOI PubMed
3. Liu Y, Zhan F, Wang B, et al. Three-dimensional composite catalysts for Al-O_2 batteries composed of $CoMn_2O_4$ Nanoneedles supported on nitrogen-doped carbon nanotubes/graphene. *ACS Appl Mater Interfaces* 2019;11:21526-35. DOI PubMed
4. Vardar G, Nelson EG, Smith JG, et al. Identifying the discharge product and reaction pathway for a secondary Mg/O_2 battery. *Chem Mater* 2015;27:7564-8. DOI
5. Li B, Zhang S, Wang B, Xia Z, Tang C, Zhang Q. A porphyrin covalent organic framework cathode for flexible Zn-air batteries. *Energy Environ Sci* 2018;11:1723-9. DOI
6. Qin L, Schkeryantz L, Zheng J, Xiao N, Wu Y. Superoxide-based K-O_2 batteries: highly reversible oxygen redox solves challenges in air electrodes. *J Am Chem Soc* 2020;142:11629-40. DOI PubMed
7. Xia C, Black R, Fernandes R, Adams B, Nazar LF. The critical role of phase-transfer catalysis in aprotic sodium oxygen batteries. *Nat Chem* 2015;7:496-501. DOI PubMed
8. Ryu WH, Gittleson FS, Thomsen JM, et al. Heme biomolecule as redox mediator and oxygen shuttle for efficient charging of lithium-oxygen batteries. *Nat Commun* 2016;7:12925. DOI PubMed PMC
9. Bruce PG, Freunberger SA, Hardwick LJ, Tarascon JM. Li-O_2 and Li-S batteries with high energy storage. *Nat Mater* 2011;11:19-29. DOI PubMed
10. Thotiyl MM, Freunberger SA, Peng Z, Chen Y, Liu Z, Bruce PG. A stable cathode for the aprotic Li-O_2 battery. *Nat Mater* 2013;12:1050-6. DOI PubMed
11. Meng F, Zhong H, Bao D, Yan J, Zhang X. In situ coupling of strung Co_4N and intertwined N-C fibers toward free-standing bifunctional cathode for robust, efficient, and flexible Zn-Air batteries. *J Am Chem Soc* 2016;138:10226-31. DOI PubMed

12. Cai X, Lai L, Lin J, Shen Z. Recent advances in air electrodes for Zn-air batteries: electrocatalysis and structural design. *Mater Horiz* 2017;4:945-76. DOI
13. Xu N, Qiao J. Recent progress in bifunctional catalysts for zinc-air batteries. *J Electrochem* 2020;26:531-562. DOI
14. Lu Z. Computational discovery of energy materials in the era of big data and machine learning: a critical review. *Materials Reports: Energy* 2021;1:100047. DOI
15. Li C, Guo Z, Yang B, Liu Y, Wang Y, Xia Y. A rechargeable Li-CO_2 battery with a gel polymer electrolyte. *Angew Chem Int Ed Engl* 2017;56:9126-30. DOI PubMed
16. Qiao Y, Yi J, Wu S, et al. Li-CO_2 Electrochemistry: a new strategy for CO_2 fixation and energy storage. *Joule* 2017;1:359-70. DOI
17. Wang T, Sang X, Zheng W, et al. Gas diffusion strategy for inserting atomic iron sites into graphitized carbon supports for unusually high-efficient CO_2 electroreduction and high-performance Zn-CO_2 batteries. *Adv Mater* 2020;32:e2002430. DOI PubMed
18. Wang K, Wu Y, Cao X, Gu L, Hu J. A Zn-CO_2 flow battery generating electricity and methane. *Adv Funct Mater* 2019;30:1908965. DOI
19. Liu B, Sun Y, Liu L, Xu S, Yan X. Advances in manganese-based oxides cathodic electrocatalysts for Li-air batteries. *Adv Funct Mater* 2018;28:1704973. DOI
20. Wang R, Chen Z, Hu N, Xu C, Shen Z, Liu J. Nanocarbon-based electrocatalysts for rechargeable aqueous Li/Zn-Air batteries. *ChemElectroChem* 2018;5:1745-63. DOI
21. Ma Z, Yuan X, Li L, et al. A review of cathode materials and structures for rechargeable lithium-air batteries. *Energy Environ Sci* 2015;8:2144-98. DOI
22. Wang Y, Lu Y. Nonaqueous lithium-oxygen batteries: reaction mechanism and critical open questions. *Energy Storage Materials* 2020;28:235-46. DOI
23. Ma L, Yu T, Tzoganakis E, et al. Fundamental understanding and material challenges in rechargeable nonaqueous Li-O_2 batteries: recent progress and perspective. *Adv Energy Mater* 2018;8:1800348. DOI
24. Balaish M, Jung J, Kim I, Ein-eli Y. A critical review on functionalization of air-cathodes for nonaqueous Li-O_2 batteries. *Adv Funct Mater* 2020;30:1808303. DOI
25. Black R, Adams B, Nazar LF. Non-aqueous and hybrid Li-O_2 batteries. *Adv Energy Mater* 2012;2:801-15. DOI
26. Wang G, Tu F, Xie J, et al. High-performance Li-O_2 batteries with controlled Li_2O_2 growth in graphene/Au-nanoparticles/Au-nanosheets sandwich. *Adv Sci (Weinh)* 2016;3:1500339. DOI PubMed PMC
27. Zhao C, Yu C, Banis MN, et al. Decoupling atomic-layer-deposition ultrafine RuO_2 for high-efficiency and ultralong-life Li-O_2 batteries. *Nano Energy* 2017;34:399-407. DOI
28. Song S, Xu W, Zheng J, et al. Complete Decomposition of Li_2CO_3 in Li-O_2 batteries using Ir/B_4C as noncarbon-based oxygen electrode. *Nano Lett* 2017;17:1417-24. DOI PubMed
29. Zhang P, Zhang S, He M, et al. Realizing the embedded growth of large Li_2O_2 aggregations by matching different metal oxides for high-capacity and high-rate lithium oxygen batteries. *Adv Sci (Weinh)* 2017;4:1700172. DOI PubMed PMC
30. Zhao W, Li X, Yin R, et al. Urchin-like NiO-$NiCo_2O_4$ heterostructure microsphere catalysts for enhanced rechargeable non-aqueous Li-O_2 batteries. *Nanoscale* 2018;11:50-9. DOI PubMed
31. Liang R, Hu A, Li M, Ran Z, Shu C, Long J. Defect regulation of heterogeneous nickel-based oxides via interfacial engineering for long-life lithium-oxygen batteries. *Electrochimica Acta* 2019;321:134716. DOI
32. Xu N, Zhang Y, Wang M, et al. High-performing rechargeable/flexible zinc-air batteries by coordinated hierarchical Bi-metallic electrocatalyst and heterostructure anion exchange membrane. *Nano Energy* 2019;65:104021. DOI
33. Xia Q, Zhao L, Zhang Z, et al. $MnCo_2S_4$-$CoS_{1.097}$ Heterostructure nanotubes as high efficiency cathode catalysts for stable and long-life lithium-oxygen batteries under high current conditions. *Adv Sci (Weinh)* 2021;8:e2103302. DOI PubMed PMC
34. Xia Q, Zhao L, Li D, et al. Phase modulation of 1T/2HMoSe_2 nanoflowers for highly efficient bifunctional electrocatalysis in rechargeable Li-O_2 batteries. *J Mater Chem A* 2021;9:19922-31. DOI
35. Hu A, Lv W, Lei T, et al. Heterostructured NiS_2/$ZnIn_2S_4$ realizing toroid-like Li_2O_2 deposition in lithium-oxygen batteries with low-donor-number solvents. *ACS Nano* 2020;14:3490-9. DOI PubMed
36. Dong S, Chen X, Zhang K, et al. Molybdenum nitride based hybrid cathode for rechargeable lithium-O_2 batteries. *Chem Commun (Camb)* 2011;47:11291-3. DOI PubMed
37. Idrees M, Batool S, Kong J, et al. Polyborosilazane derived ceramics - nitrogen sulfur dual doped graphene nanocomposite anode for enhanced lithium ion batteries. *Electrochimica Acta* 2019;296:925-37. DOI
38. Lee G, Sung M, Kim J, Song HJ, Kim D. Synergistic effect of $CuGeO_3$/graphene composites for efficient oxygen-electrode electrocatalysts in Li-O_2 batteries. *Adv Energy Mater* 2018;8:1801930. DOI
39. Tan G, Chong L, Amine R, et al. Toward highly efficient electrocatalyst for Li-O_2 batteries using biphasic N-doping cobalt@graphene multiple-capsule heterostructures. *Nano Lett* 2017;17:2959-66. DOI PubMed
40. Xu JJ, Wang ZL, Xu D, Zhang LL, Zhang XB. Tailoring deposition and morphology of discharge products towards high-rate and long-life lithium-oxygen batteries. *Nat Commun* 2013;4:2438. DOI PubMed
41. Mou S, Wu T, Xie J, et al. Boron phosphide nanoparticles: a nonmetal catalyst for high-selectivity electrochemical reduction of CO_2 to CH_3OH. *Adv Mater* 2019;31:e1903499. DOI PubMed
42. Beck A, Huang X, Artiglia L, et al. The dynamics of overlayer formation on catalyst nanoparticles and strong metal-support interaction. *Nat Commun* 2020;11:3220. DOI PubMed PMC

43. Kwon O, Sengodan S, Kim K, et al. Exsolution trends and co-segregation aspects of self-grown catalyst nanoparticles in perovskites. *Nat Commun* 2017;8:15967. DOI PubMed PMC
44. Higaki T, Li Y, Zhao S, et al. Atomically tailored gold nanoclusters for catalytic application. *Angew Chem Int Ed Engl* 2019;58:8291-302. DOI PubMed
45. Rong W, Zou H, Zang W, et al. Size-dependent activity and selectivity of atomic-level copper nanoclusters during CO/CO_2 electroreduction. *Angew Chem Int Ed Engl* 2021;60:466-72. DOI PubMed
46. Zhao J, Jin R. Heterogeneous catalysis by gold and gold-based bimetal nanoclusters. *Nano Today* 2018;18:86-102. DOI
47. Qiao B, Wang A, Yang X, et al. Single-atom catalysis of CO oxidation using Pt1/FeOx. *Nat Chem* 2011;3:634-41. DOI PubMed
48. Peng Y, Lu B, Chen S. Carbon-supported single atom catalysts for electrochemical energy conversion and storage. *Adv Mater* 2018;30:e1801995. DOI PubMed
49. Li S, Hao X, Abudula A, Guan G. Nanostructured Co-based bifunctional electrocatalysts for energy conversion and storage: current status and perspectives. *J Mater Chem A* 2019;7:18674-707. DOI
50. Sun T, Xu L, Wang D, Li Y. Metal organic frameworks derived single atom catalysts for electrocatalytic energy conversion. *Nano Res* 2019;12:2067-80. DOI
51. Zhu C, Shi Q, Xu BZ, et al. Hierarchically porous M-N-C (M = Co and Fe) single-atom electrocatalysts with robust MN_x active moieties enable enhanced ORR performance. *Adv Energy Mater* 2018;8:1801956. DOI
52. Wang Y, Li Q, Zhang L, et al. A gel-limiting strategy for large-scale fabrication of Fe-N-C single-atom ORR catalysts. *J Mater Chem A* 2021;9:7137-42. DOI
53. Liu F, Yan N, Zhu G, et al. Fe-N-C single-atom catalysts with an axial structure prepared by a new design and synthesis method for ORR. *New J Chem* 2021;45:13004-14. DOI
54. Tavakkoli M, Flahaut E, Peljo P, et al. Mesoporous single-atom-doped grapheme-carbon nanotube hybrid: synthesis and tunable electrocatalytic activity for oxygen evolution and reduction reactions. *ACS Catal* 2020;10:4647-58. DOI
55. Deng Q, Zhao J, Wu T, Chen G, Hansen HA, Vegge T. 2D transition metal-TCNQ sheets as bifunctional single-atom catalysts for oxygen reduction and evolution reaction (ORR/OER). *J Catal* 2019;370:378-84. DOI
56. Ying Y, Fan K, Luo X, Qiao J, Huang H. Unravelling the origin of bifunctional OER/ORR activity for single-atom catalysts supported on C_2N by DFT and machine learning. *J Mater Chem A* 2021;9:16860-7. DOI
57. Zhu C, Shi Q, Feng S, Du D, Lin Y. Single-atom catalysts for electrochemical water splitting. *ACS Energy Lett* 2018;3:1713-21. DOI
58. Zeng L, Dai C, Liu B, Xue C. Oxygen-assisted stabilization of single-atom Au during photocatalytic hydrogen evolution. *J Mater Chem A* 2019;7:24217-21. DOI
59. Zhang J, Xu X, Yang L, Cheng D, Cao D. Single-atom Ru doping induced phase transition of MoS_2 and S vacancy for hydrogen evolution reaction. *Small Methods* 2019;3:1900653. DOI
60. Gao D, Liu T, Wang G, Bao X. Structure sensitivity in single-atom catalysis toward CO_2 electroreduction. *ACS Energy Lett* 2021;6:713-27. DOI
61. Li M, Wang H, Luo W, Sherrell PC, Chen J, Yang J. Heterogeneous single-atom catalysts for electrochemical CO_2 reduction reaction. *Adv Mater* 2020;32:e2001848. DOI PubMed
62. Cao S, Wei S, Wei X, et al. Can N, S cocoordination promote single atom catalyst performance in CO_2RR? *Small* 2021;17:e2100949. DOI
63. Dopilka A, Zhao R, Weller JM, Bobev S, Peng X, Chan CK. Experimental and computational study of the lithiation of $Ba_8Al_yGe_{46-y}$ based type I germanium clathrates. *ACS Appl Mater Interfaces* 2018;10:37981-93. DOI PubMed
64. Lee YW, Kim DM, Kim SJ, et al. In situ synthesis and characterization of Ge embedded electrospun carbon nanostructures as high performance anode material for lithium-ion batteries. *ACS Appl Mater Interfaces* 2016;8:7022-9. DOI PubMed
65. Ma W, Wang Y, Yang Y, et al. Temperature-dependent Li storage performance in nanoporous Cu-Ge-Al alloy. *ACS Appl Mater Interfaces* 2019;11:9073-82. DOI PubMed
66. Yu J, Li B, Zhao C, Zhang Q. Seawater electrolyte-based metal-air batteries: from strategies to applications. *Energy Environ Sci* 2020;13:3253-68. DOI
67. Sun Y, Liu X, Jiang Y, et al. Recent advances and challenges in divalent and multivalent metal electrodes for metal-air batteries. *J Mater Chem A* 2019;7:18183-208. DOI
68. Liu Q, Chang Z, Li Z, Zhang X. Flexible metal-air batteries: progress, challenges, and perspectives. *Small Methods* 2018;2:1700231. DOI
69. Watanabe M, Thomas ML, Zhang S, Ueno K, Yasuda T, Dokko K. Application of ionic liquids to energy storage and conversion materials and devices. *Chem Rev* 2017;117:7190-239. DOI PubMed
70. Lyu Z, Zhou Y, Dai W, et al. Recent advances in understanding of the mechanism and control of Li_2O_2 formation in aprotic Li-O_2 batteries. *Chem Soc Rev* 2017;46:6046-72. DOI
71. Li Y, Lu J. Metal-air batteries: will they be the future electrochemical energy storage device of choice? *ACS Energy Lett* 2017;2:1370-7. DOI
72. Ma L, Chen S, Wang D, et al. Super-stretchable zinc-air batteries based on an alkaline-tolerant dual-network hydrogel electrolyte. *Adv Energy Mater* 2019;9:1803046. DOI
73. Zhang Y, Wu Y, You W, et al. Deeply rechargeable and hydrogen-evolution-suppressing zinc anode in alkaline aqueous electrolyte. *Nano Lett* 2020;20:4700-7. DOI PubMed

74. Zhong C, Liu B, Ding J, et al. Decoupling electrolytes towards stable and high-energy rechargeable aqueous zinc-manganese dioxide batteries. *Nat Energy* 2020;5:440-9. DOI
75. Lu J, Li L, Park JB, Sun YK, Wu F, Amine K. Aprotic and aqueous Li-O_2 batteries. *Chem Rev* 2014;114:5611-40. DOI PubMed
76. Pan J, Xu YY, Yang H, Dong Z, Liu H, Xia BY. Advanced architectures and relatives of air electrodes in zn-air batteries. *Adv Sci (Weinh)* 2018;5:1700691. DOI PubMed PMC
77. Lee J, Hwang B, Park M, Kim K. Improved reversibility of Zn anodes for rechargeable Zn-air batteries by using alkoxide and acetate ions. *Electrochimica Acta* 2016;199:164-71. DOI
78. Zhang Y, Deng Y, Wang J, et al. Recent progress on flexible Zn-air batteries. *Energy Storage Materials* 2021;35:538-49. DOI
79. Zhong Y, Xu X, Wang W, Shao Z. Recent advances in metal-organic framework derivatives as oxygen catalysts for zinc-air batteries. *Batteries & Supercaps* 2019;2:272-89. DOI
80. Zhao Z, Fan X, Ding J, Hu W, Zhong C, Lu J. Challenges in zinc electrodes for alkaline zinc-air batteries: obstacles to commercialization. *ACS Energy Lett* 2019;4:2259-70. DOI
81. Zelger C, Süßenbacher M, Laskos A, Gollas B. State of charge indicators for alkaline zinc-air redox flow batteries. *Journal of Power Sources* 2019;424:76-81. DOI
82. Xie J, Wang Y. Recent development of CO_2 electrochemistry from Li-CO_2 batteries to Zn-CO_2 batteries. *Acc Chem Res* 2019;52:1721-9. DOI PubMed
83. Chen Y, Mei Y, Li M, et al. Highly selective CO_2 conversion to methane or syngas tuned by CNTs@non-noble-metal cathodes in Zn-CO_2 flow batteries. *Green Chem* 2021;23:8138-46. DOI
84. Gao S, Jin M, Sun J, et al. Coralloid Au enables high-performance Zn-CO_2 battery and self-driven CO production. *J Mater Chem A* 2021;9:21024-31. DOI
85. Liu X, Tao S, Zhang J, Zhu Y, Ma R, Lu J. Ultrathin p-n type Cu_2O/CuCoCr-layered double hydroxide heterojunction nanosheets for photo-assisted aqueous Zn-CO_2 batteries. *J Mater Chem A* 2021;9:26061-8. DOI
86. Xie J, Wang X, Lv J, et al. Reversible aqueous zinc-CO_2 batteries based on CO_2-HCOOH interconversion. *Angew Chem Int Ed Engl* 2018;57:16996-7001. DOI
87. Kwak WJ, Rosy, Sharon D, et al. Lithium-oxygen batteries and related systems: potential, status, and future. *Chem Rev* 2020;120:6626-83. DOI PubMed
88. Aurbach D, Mccloskey BD, Nazar LF, Bruce PG. Advances in understanding mechanisms underpinning lithium-air batteries. *Nat Energy* 2016:1. DOI
89. Chang Z, Xu J, Liu Q, Li L, Zhang X. Recent progress on stability enhancement for cathode in rechargeable non-aqueous lithium-oxygen battery. *Adv Energy Mater* 2015;5:1500633. DOI
90. Lyu Z, Yang L, Luan Y, et al. Effect of oxygen adsorbability on the control of Li_2O_2 growth in Li-O_2 batteries: implications for cathode catalyst design. *Nano Energy* 2017;36:68-75. DOI
91. Li F, Chen J. Mechanistic evolution of aprotic lithium-oxygen batteries. *Adv Energy Mater* 2017;7:1602934. DOI
92. Takechi K, Shiga T, Asaoka T. A Li-O_2/CO_2 battery. *Chem Commun (Camb)* 2011;47:3463-5. DOI PubMed
93. Hu A, Shu C, Xu C, et al. Design strategies toward catalytic materials and cathode structures for emerging Li-CO_2 batteries. *J Mater Chem A* 2019;7:21605-33. DOI
94. Mu X, Pan H, He P, Zhou H. Li-CO_2 and Na-CO_2 batteries: toward greener and sustainable electrical energy storage. *Adv Mater* 2020;32:e1903790. DOI PubMed
95. Li X, Yang S, Feng N, He P, Zhou H. Progress in research on Li-CO_2 batteries: mechanism, catalyst and performance. *Chinese J Catal* 2016;37:1016-24. DOI
96. Jiao Y, Qin J, Sari HMK, Li D, Li X, Sun X. Recent progress and prospects of Li-CO_2 batteries: mechanisms, catalysts and electrolytes. *Energy Stor Mater* 2021;34:148-70. DOI
97. Mitchell S, Pérez-Ramírez J. Single atom catalysis: a decade of stunning progress and the promise for a bright future. *Nat Commun* 2020;11:4302. DOI PubMed PMC
98. Zhang L, Wang Y, Niu Z, Chen J. Single atoms on graphene for energy storage and conversion. *Small Methods* 2019;3:1800443. DOI
99. Zhu C, Fu S, Shi Q, Du D, Lin Y. Single-atom electrocatalysts. *Angew Chem Int Ed Engl* 2017;56:13944-60. DOI PubMed
100. Yang XF, Wang A, Qiao B, Li J, Liu J, Zhang T. Single-atom catalysts: a new frontier in heterogeneous catalysis. *Acc Chem Res* 2013;46:1740-8. DOI PubMed
101. Ma L, Zhu G, Wang D, et al. Emerging metal single atoms in electrocatalysts and batteries. *Adv Funct Mater* 2020;30:2003870. DOI
102. Zhang Z, Zhao X, Xi S, et al. Atomically dispersed cobalt trifunctional electrocatalysts with tailored coordination environment for flexible rechargeable Zn-air battery and self-driven water splitting. *Adv Energy Mater* 2020;10:2002896. DOI
103. Sun H, Wang M, Zhang S, et al. Boosting oxygen dissociation over bimetal sites to facilitate oxygen reduction activity of zinc-air battery. *Adv Funct Mater* 2021;31:2006533. DOI
104. Zhao L, Rong X, Niu Y, et al. Ostwald ripening tailoring hierarchically porous $Na_3V_2(PO_4)_2O_2F$ hollow nanospheres for superior high-rate and ultrastable sodium ion storage. *Small* 2020;16:e2004925. DOI
105. Li L, Chang X, Lin X, Zhao ZJ, Gong J. Theoretical insights into single-atom catalysts. *Chem Soc Rev* 2020;49:8156-78. DOI PubMed
106. Zheng Y, Jiao Y, Zhu Y, et al. Molecule-level g-C_3N_4 coordinated transition metals as a new class of electrocatalysts for oxygen

electrode reactions. *J Am Chem Soc* 2017;139:3336-9. DOI PubMed

107. Huang D, Luo Y, Li S, et al. Recent advances in tuning the electronic structures of atomically dispersed M-N-C materials for efficient gas-involving electrocatalysis. *Mater Horiz* 2020;7:970-86. DOI
108. Hossain MD, Liu Z, Zhuang M, et al. Rational design of grapheme-supported single atom catalysts for hydrogen evolution reaction. *Adv Energy Mater* 2019;9:1803689. DOI
109. Wang X, Chen Z, Zhao X, et al. Regulation of coordination number over single Co sites: triggering the efficient electroreduction of CO_2. *Angew Chem Int Ed Engl* 2018;57:1944-8. DOI PubMed
110. Pan F, Zhang H, Liu K, et al. Unveiling active sites of CO_2 reduction on nitrogen-coordinated and atomically dispersed iron and cobalt catalysts. *ACS Catal* 2018;8:3116-22. DOI
111. Yuan K, Sfaelou S, Qiu M, et al. Synergetic contribution of boron and Fe-Nx species in porous carbons toward efficient electrocatalysts for oxygen reduction reaction. *ACS Energy Lett* 2018;3:252-60. DOI
112. Ren W, Tan X, Yang W, et al. Isolated diatomic Ni-Fe metal-nitrogen sites for synergistic electroreduction of CO_2. *Angew Chem Int Ed Engl* 2019;58:6972-6. DOI PubMed
113. Osmieri L, Escudero-cid R, Monteverde Videla AH, Ocón P, Specchia S. Performance of a Fe-N-C catalyst for the oxygen reduction reaction in direct methanol fuel cell: cathode formulation optimization and short-term durability. *Applied Catalysis B: Environmental* 2017;201:253-65. DOI
114. Fei H, Dong J, Feng Y, et al. General synthesis and definitive structural identification of MN_4C_4 single-atom catalysts with tunable electrocatalytic activities. *Nat Catal* 2018;1:63-72. DOI
115. Du C, Gao Y, Wang J, Chen W. A new strategy for engineering a hierarchical porous carbon-anchored Fe single-atom electrocatalyst and the insights into its bifunctional catalysis for flexible rechargeable Zn-air batteries. *J Mater Chem A* 2020;8:9981-90. DOI
116. Chen G, Liu P, Liao Z, et al. Zinc-mediated template synthesis of Fe-N-C electrocatalysts with densely accessible Fe-N_x active sites for efficient oxygen reduction. *Adv Mater* 2020;32:e1907399. DOI PubMed
117. Zeng Z, Yi L, He J, et al. Hierarchically porous carbon with pentagon defects as highly efficient catalyst for oxygen reduction and oxygen evolution reactions. *J Mater Sci* 2020;55:4780-91. DOI
118. Ji D, Fan L, Li L, et al. Atomically transition metals on self-supported porous carbon flake arrays as binder-free air cathode for wearable zinc-air batteries. *Adv Mater* 2019;31:e1808267. DOI PubMed
119. Han X, Ling X, Wang Y, et al. Generation of nanoparticle, atomic-cluster, and single-atom cobalt catalysts from zeolitic imidazole frameworks by spatial isolation and their use in zinc-air batteries. *Angew Chem Int Ed Engl* 2019;58:5359-64. DOI PubMed
120. Wu H, Li H, Zhao X, et al. Highly doped and exposed Cu(i)-N active sites within graphene towards efficient oxygen reduction for zinc-air batteries. *Energy Environ Sci* 2016;9:3736-45. DOI
121. Yang Y, Wang C, Gao S, et al. Incorporation of Cu-N_x cofactors into graphene encapsulated Co as biomimetic electrocatalysts for efficient oxygen reduction. *Nanoscale* 2018;10:21076-86. DOI PubMed
122. Sun H, Liu S, Wang M, Qian T, Xiong J, Yan C. Updating the intrinsic activity of a single-atom site with a P-O bond for a rechargeable Zn-air battery. *ACS Appl Mater Interfaces* 2019;11:33054-61. DOI PubMed
123. Chen Y, Ji S, Zhao S, et al. Enhanced oxygen reduction with single-atomic-site iron catalysts for a zinc-air battery and hydrogen-air fuel cell. *Nat Commun* 2018;9:5422. DOI PubMed PMC
124. Yang Y, Mao K, Gao S, et al. O-, N-atoms-coordinated Mn cofactors within a graphene framework as bioinspired oxygen reduction reaction electrocatalysts. *Adv Mater* 2018;30:e1801732. DOI PubMed
125. Han X, Ling X, Yu D, et al. Atomically dispersed binary Co-Ni sites in nitrogen-doped hollow carbon nanocubes for reversible oxygen reduction and evolution. *Adv Mater* 2019;31:e1905622. DOI PubMed
126. Zhu X, Zhang D, Chen C, et al. Harnessing the interplay of Fe-Ni atom pairs embedded in nitrogen-doped carbon for bifunctional oxygen electrocatalysis. *Nano Energy* 2020;71:104597. DOI
127. Gong S, Wang C, Jiang P, Hu L, Lei H, Chen Q. Designing highly efficient dual-metal single-atom electrocatalysts for the oxygen reduction reaction inspired by biological enzyme systems. *J Mater Chem A* 2018;6:13254-62. DOI
128. Zheng W, Yang J, Chen H, et al. Atomically defined undercoordinated active sites for highly efficient CO_2 electroreduction. *Adv Funct Mater* 2019;30:1907658. DOI
129. Yang R, Xie J, Liu Q, et al. A trifunctional Ni-N/P-O-codoped graphene electrocatalyst enables dual-model rechargeable Zn-CO_2/Zn-O_2 batteries. *J Mater Chem A* 2019;7:2575-80. DOI
130. Wang P, Ren Y, Wang R, et al. Atomically dispersed cobalt catalyst anchored on nitrogen-doped carbon nanosheets for lithium-oxygen batteries. *Nat Commun* 2020;11:1576. DOI PubMed PMC
131. Shui JL, Karan NK, Balasubramanian M, Li SY, Liu DJ. Fe/N/C composite in Li-O_2 battery: studies of catalytic structure and activity toward oxygen evolution reaction. *J Am Chem Soc* 2012;134:16654-61. DOI PubMed
132. Song LN, Zhang W, Wang Y, et al. Tuning lithium-peroxide formation and decomposition routes with single-atom catalysts for lithium-oxygen batteries. *Nat Commun* 2020;11:2191. DOI PubMed PMC
133. Hu X, Luo G, Zhao Q, et al. Ru single atoms on N-doped carbon by spatial confinement and ionic substitution strategies for high-performance Li-O_2 batteries. *J Am Chem Soc* 2020;142:16776-86. DOI PubMed
134. Zhao W, Wang J, Yin R, et al. Single-atom Pt supported on holey ultrathin g-C_3N_4 nanosheets as efficient catalyst for Li-O_2 batteries. *J Colloid Interface Sci* 2020;564:28-36. DOI PubMed
135. Hu C, Gong L, Xiao Y, et al. High-performance, long-life, rechargeable Li-CO_2 batteries based on a 3D holey graphene cathode

implanted with single iron atoms. *Adv Mater* 2020;32:e1907436. DOI PubMed

136. Zhang B, Jiao Y, Chao D, et al. Targeted synergy between adjacent Co atoms on graphene oxide as an efficient new electrocatalyst for Li-CO_2 batteries. Adv Funct Mater 2019;29:1904206. DOI
137. Zang W, Sumboja A, Ma Y, et al. Single Co atoms anchored in porous N-doped carbon for efficient zinc-air battery cathodes. *ACS Catal* 2018;8:8961-9. DOI
138. Yang ZK, Yuan C, Xu A. Confined pyrolysis within a nanochannel to form a highly efficient single iron site catalyst for Zn-air batteries. *ACS Energy Lett* 2018;3:2383-9. DOI
139. Li BQ, Zhao CX, Chen S, et al. Framework-porphyrin-derived single-atom bifunctional oxygen electrocatalysts and their applications in Zn-air batteries. *Adv Mater* 2019;31:e1900592. DOI PubMed
140. Qiu HJ, Du P, Hu K, et al. Metal and nonmetal codoped 3D nanoporous graphene for efficient bifunctional electrocatalysis and rechargeable Zn-air batteries. *Adv Mater* 2019;31:e1900843. DOI PubMed
141. Tang C, Wang B, Wang HF, Zhang Q. Defect engineering toward atomic Co-N_x-C in hierarchical graphene for rechargeable flexible solid Zn-air batteries. *Adv Mater* 2017;29:1703185. DOI PubMed
142. Wu J, Zhou H, Li Q, et al. Densely populated isolated single CoN site for efficient oxygen electrocatalysis. *Adv Energy Mater* 2019;9:1900149. DOI
143. Pan Y, Liu S, Sun K, et al. A bimetallic Zn/Fe polyphthalocyanine-derived single-atom Fe-N_4 catalytic site:a superior trifunctional catalyst for overall water splitting and Zn-air batteries. *Angew Chem Int Ed Engl* 2018;57:8614-8. DOI PubMed
144. Wagh NK, Shinde SS, Lee CH, et al. Densely colonized isolated Cu-N single sites for efficient bifunctional electrocatalysts and rechargeable advanced Zn-air batteries. *Appl Catal B: Environ* 2020;268:118746. DOI
145. Zhao J, Qin R, Liu R. Urea-bridging synthesis of nitrogen-doped carbon tube supported single metallic atoms as bifunctional oxygen electrocatalyst for zinc-air battery. *Applied Catalysis B: Environmental* 2019;256:117778. DOI
146. Zhang J, Liu Y, Yu Z, et al. Boosting the performance of the Fe-N-C catalyst for the oxygen reduction reaction by introducing single-walled carbon nanohorns as branches on carbon fibers. *J Mater Chem A* 2019;7:23182-90. DOI
147. Yang L, Shi L, Wang D, Lv Y, Cao D. Single-atom cobalt electrocatalysts for foldable solid-state Zn-air battery. *Nano Energy* 2018;50:691-8. DOI
148. Zhang X, Han X, Jiang Z, et al. Atomically dispersed hierarchically ordered porous Fe-N-C electrocatalyst for high performance electrocatalytic oxygen reduction in Zn-Air battery. *Nano Energy* 2020;71:104547. DOI
149. Yang ZK, Yuan CZ, Xu AW. A rationally designed Fe-tetrapyridophenazine complex: a promising precursor to a single-atom Fe catalyst for an efficient oxygen reduction reaction in high-power Zn-air cells. *Nanoscale* 2018;10:16145-52. DOI PubMed
150. Lyu X, Li G, Chen X, et al. Atomic cobalt on defective bimodal mesoporous carbon toward efficient oxygen reduction for zinc-air batteries. *Small Methods* 2019;3:1800450. DOI
151. Wang J, Liu W, Luo G, et al. Synergistic effect of well-defined dual sites boosting the oxygen reduction reaction. *Energy Environ Sci* 2018;11:3375-9. DOI
152. Zheng W, Chen F, Zeng Q, et al. A universal principle to accurately synthesize atomically dispersed metal-N_4 sites for CO_2 electroreduction. *Nanomicro Lett* 2020;12:108. DOI PubMed PMC
153. Hai X, Xi S, Mitchell S, et al. Scalable two-step annealing method for preparing ultra-high-density single-atom catalyst libraries. *Nat Nanotechnol* 2022;17:174-81. DOI PubMed